International Journal for Numerical and Analytical Methods in Geomechanics

WILEY

RESEARCH ARTICLE OPEN ACCESS

Neohypoplasticity for Sand Coupled With the Generalized Intergranular Strain Concept

Luis Mugele[1] | Hans Henning Stutz[1] | David Mašín[2]

[1]Karlsruhe Institute of Technology (KIT), Institute of Soil Mechanics and Rock Mechanics (IBF), Karlsruhe, Germany | [2]Faculty of Science, Charles University, Praha, Czech Republic

Correspondence: Luis Mugele (luis.mugele@kit.edu)

Received: 4 December 2024 | **Revised:** 23 June 2025 | **Accepted:** 19 July 2025

Funding: Financial support was provided by the research travel grant from Karlsruhe House of Young Scientists (KHYS) and grant INTER-COST No. LUC24143 of the Czech Ministry of Education, Youth and Sports.

Keywords: bifurcation | cyclic loading | fabric | generalized intergranular strain | neohypoplasticity | sand

ABSTRACT

This work presents the coupling of the recently revisited advanced hypoplastic constitutive sand model called neohypoplasticity (NHP) with the more recently introduced concept of the generalized intergranular strain (GIS) to account for soil behavior due to small strains. The latter is essential for the simulation of cyclic deformations. In addition to the effective Cauchy-stress $\boldsymbol{\sigma}$ and the void ratio e, the resulting NHP+GIS formulation includes a fabric tensor $\boldsymbol{z}$ (to account for the anisotropic soil structure), the intergranular strain $\boldsymbol{h}$, and a cyclic preloading variable Ω as state variables. The parameter calibration of the 11 NHP and 10 GIS parameters is discussed in detail and significantly simplified compared to previous NHP versions. Element test simulations of monotonic and cyclic tests and their comparison with experimental data from Karlsruhe fine sand (KFS) and Zbraslav sand (ZS) reveal the satisfying performance of the novel model. The NHP+GIS model captures soil anisotropy effects and static liquefaction in loose sand. Cyclic mobility can be modeled irrespective of soil density. Finally, the NHP+GIS model is applied to a bifurcation problem under plane strain conditions, demonstrating its applicability in initial boundary value problems.

1 | Introduction

Numerous constitutive models have been developed in the last decades for the mathematical description of the mechanical behavior of soil. Advanced constitutive formulations can be used nowadays to simulate the main characteristics of soil behavior due to monotonic deformation including density dependency (pyknotropy) and pressure dependency (barotropy). With extensions for considering the effects due to a reversal in the loading direction, so-called small strain effects, modern constitutive models can also be used to simulate the cyclic soil behavior.

Especially hypoplastic constitutive models have proven to be particularly suitable for simulating soil. These models predict irreversible deformations within the whole stress space due to the lack of a fully elastic region. The rate of the effective Cauchy-stress $\dot{\boldsymbol{\sigma}}$ (objective Zaremba-Jaumann rate $\mathring{\boldsymbol{\sigma}}$ to be precise) can be expressed in hypoplastic models using a single tensorial equation with the strain rate $\dot{\boldsymbol{\varepsilon}}$ (Euler stretching tensor $\boldsymbol{D}$ to be precise). A decomposition of the strain rate into an elastic and a plastic part, as known from elasto-plasticity, does not exist in hypoplastic models. No yield surface, no plastic potential, and no plastic multiplier need to be defined. A comprehensive overview

Abbreviations: ASBS, asymptotic state boundary surface; BVP, boundary value problem; CP, cyclic preloading; GIS, generalized intergranular strain; HP, hypoplasticity after von Wolffersdorff; IP, integration point; IS, intergranular strain after Niemunis and Herle; ISI, intergranular strain improvement; KFS, Karlsruhe fine sand; NHP, neohypoplasticity; ZS, Zbraslav sand.

of the evolution of hypoplastic models in the past decades can be found in the literature [1–3].

Based on the generalized hypoplasticity proposed by Niemunis [4], an extended generalized hypoplasticity was recently proposed for rate-independent hypoplastic constitutive models [5]:

$$\dot{\boldsymbol{\sigma}} = \mathsf{E} : (\dot{\boldsymbol{\varepsilon}} - \boldsymbol{m}\, C\, S\, \|\dot{\boldsymbol{\varepsilon}}\| + \boldsymbol{f}(\dot{\boldsymbol{\varepsilon}}, \boldsymbol{\alpha}))\,. \tag{1}$$

In Equation (1), E represents the elastic stiffness tensor, $\boldsymbol{m}$ the hypoplastic equivalent flow rule, C a scalar multiplier, and S the so-called state mobilization. The novelty of Equation (1) comes from this state mobilization S, which indicates whether the current state of the soil is located on the so-called asymptotic state boundary surface (ASBS) or not ($S = 1$ or $S \neq 1$).

The tensor-valued function $\boldsymbol{f}(\dot{\boldsymbol{\varepsilon}}, \boldsymbol{\alpha})$ is introduced for generalization and must be homogeneous of first degree in the strain rate to ensure rate-independent constitutive behavior. Additional state variables are denoted as $\boldsymbol{\alpha}$. Note that rate-dependent hypoplastic constitutive formulations, such as [4, 6, 7], are beyond the scope of this paper.

The characteristic incremental nonlinearity, that, the continuous dependency of the tangent stiffness on the direction of the applied strain rate [8], of hypoplastic models is implied by the norm of the strain rate $\|\dot{\boldsymbol{\varepsilon}}\|$ in Equation (1). Note that an additional nonlinearity can be induced by the term $\boldsymbol{f}(\dot{\boldsymbol{\varepsilon}}, \boldsymbol{\alpha})$.[1] As demonstrated by Mugele et al. [5], numerous existing rate-independent hypoplastic formulations can be expressed in terms of Equation (1). For hypoplastic models for coarse-grained soils, one can refer to [9–14], while formulations for fine-grained soils can be found in [15–18].

For the simulation of monotonic deformations of sand, the hypoplastic model after von Wolffersdorff (HP) [9] is widely accepted despite existing and known deficits. To address some of them due to cyclic deformation (e.g., the so-called ratcheting), Niemunis and Herle [19] extended the model by the intergranular strain (IS) concept. The resulting coupled HP+IS formulation is nowadays widely used in geotechnical simulations considering monotonic as well as cyclic deformations [20–23].

However, both parts of the HP+IS constitutive model still exhibit several shortcomings [5, 23–26]. For the HP (a) an insufficient reproduction of dilatancy effects, (b) potential access to tensile stress states in dense conditions, (c) the hypoelastic stiffness tensor E, and (d) the nonconsideration of the effect from an anisotropic microstructure (also known as fabric or structure) on the overall mechanical behavior should be mentioned.

In addition, the IS extension shows (e) the so-called overshooting, (f) potential access to tensile stress states due to multiple deformation cycles, and (g) an inadequate reproduction of accumulation effects. Depending on the parameter calibration, the HP+IS can also exhibit (h) undershooting issues and (i) an unrealistic simulation of hysteretic and damping behavior. It is also worth mentioning that, strictly speaking, the HP+IS formulation is incrementally bilinear [8].

The mentioned shortcomings of the HP have been addressed in the recently revisited neohypoplasticity (NHP) [24, 27, 28]. The major limitations of the IS extension could be mitigated within the framework of the generalized intergranular strain (GIS) concept [5] by a reinterpretation and a combination of several improvements of the original IS concept from the literature [29–32]. As the GIS concept is based on Equation (1), it can be applied in a straightforward procedure to various hypoplastic constitutive formulations. However, only its coupling with the HP model, resulting in the HP+GIS formulation [5], has been investigated until now.

In this paper, the coupled hypoplastic model NHP+GIS is presented and the calibration of related constitutive parameters is discussed. The feasibility of the novel NHP+GIS constitutive formulation is demonstrated using element test simulations and their comparison with experimental data of both Karlsruhe fine sand (KFS) and Zbraslav sand (ZS). Remaining issues of the model are discussed. Subsequently, the constitutive formulation is used in a finite element analysis of the formation of a shear band (bifurcation) under 2D plane strain conditions. It should be noted that this paper uses the sign convention of general mechanics (compression negative) and the notation is described in detail in Appendix A.

2 | Neohypoplasticity (NHP)

The recently revisited hypoplastic constitutive model for sand called neohypoplasticity (NHP) [24, 27, 28] mitigates some of the mentioned shortcomings of earlier hypoplastic models for sand. The improvements include (a) a hyperelastic linear stiffness, (b) an explicitly defined degree of nonlinearity, (c) an accurate description of dilatancy effects, and (d) an evolving additional state variable accounting for the current anisotropic fabric of the soil. The NHP is briefly described hereinafter, whereby some improvements compared to the NHP version of [24] are introduced and described in detail. The reader is also referred to the literature [24, 27, 28] and Appendix B summarizing all governing equations and providing a list of the most important symbols. In NHP, the rate of the effective Cauchy-stress $\dot{\boldsymbol{\sigma}}$ can be expressed as a single tensorial function of the strain rate $\dot{\boldsymbol{\varepsilon}}$ as

$$\dot{\boldsymbol{\sigma}} = \overline{\mathsf{E}} : \left(\dot{\boldsymbol{\varepsilon}} - \boldsymbol{m} Y \|\dot{\boldsymbol{\varepsilon}}\| - \boldsymbol{m}^z Y_z \|\dot{\boldsymbol{\varepsilon}}\| - \boldsymbol{m}^d Y_d \|\dot{\boldsymbol{\varepsilon}}\|\right) \tag{2}$$

including the elastic stiffness $\overline{\mathsf{E}}$, the hypoplastic equivalent flow rule $\boldsymbol{m}$, and the degree of nonlinearity Y. The elastic stiffness is derived using a complementary energy function

$$\bar{\psi}(\boldsymbol{\sigma}) = P_0\, c \left(\frac{P}{P_0}\right)^{\alpha} \left(\frac{R}{P_0}\right)^{2-n-\alpha} \tag{3}$$

with $P = -\operatorname{tr}(\boldsymbol{\sigma})/\sqrt{3}$ and $R = \|\boldsymbol{\sigma}\|$ including three constitutive parameters c, α, and n and a reference pressure $P_0 = 1$ kPa. The parameter n specifies the stress homogeneity of the stiffness and c scales the latter. α can be correlated with the Poisson ratio for an isotropic stress state [26]. It should be noted that the normalization using the reference pressure P_0 is essential to attain unit consistency [11], but is often omitted in the literature [24, 28, 33]. The resulting stress-dependent hyperelastic stiffness tensor

E is further modified to $\overset{\circ}{\overline{\mathsf{E}}}$ to account for different soil behavior for loose and dense samples in dependence of the current fabric tensor $\boldsymbol{z}$. The governing equations can be found in Appendix B. This modification leads to a loss of the hyperelastic characteristic. However, the stiffness $\overset{\circ}{\overline{\mathsf{E}}}$ becomes hyperelastic in the critical state and during small stress or strain cycles due to a shakedown of the state variables. The benefits of a hyperelastic stiffness compared with a hypoelastic one are discussed in Appendix C. The limit void ratios for the densest state $e_d(P)$, the critical state $e_c(P)$, and the loosest state $e_i(P)$ are pressure-dependent and incorporated in the NHP according to the compression law after Bauer [10]:

$$\frac{e_i}{e_{i0}} = \frac{e_d}{e_{d0}} = \frac{e_c}{e_{c0}} = \exp\left[-\left(\frac{\sqrt{3}P}{h_s}\right)^{n_B}\right]. \tag{4}$$

Equation (4) includes the parameters e_{i0}, e_{c0}, e_{d0}, h_s, and n_B. A volume constant proportional strain path leads asymptotically to the critical state with the critical void ratio $e_c(P)$ according to Equation (4). Note that other proportional strain paths tend, in NHP, to states which cannot be described by Equation (4).

Some modifications to the version of NHP in [24] are proposed in this paper, based on the intensive parameter studies performed. First, a direct density dependency of the stiffness $\overline{\mathsf{E}}$ is included. The factor

$$F_e(e) = 1 + k_e\left\langle\frac{e_c(P) - e}{e_c(P) - e_d(P)}\right\rangle \tag{5}$$

is defined as a function of the current void ratio e and the limit void ratios $e_c(P)$ and $e_d(P)$ with the controlling parameter k_e. The higher the void ratio, the lower the factor F_e and the lower the scaled stiffness according to

$$\overline{\mathsf{E}} = F_e(e)\,\overset{\circ}{\overline{\mathsf{E}}}. \tag{6}$$

In the critical state, $e = e_c(P)$ holds and therefore $F_e = 1$ applies. For $e < e_c(P)$ applies $F_e > 1$ and for $e > e_c(P)$, it is ensured by $F_e = 1$ that the stiffness does not become unrealistically small or even negative.

The degree of nonlinearity Y defines the intensity of the irreversible deformations and is defined based on the Matsuoka–Nakai criterion [34]:

$$F_{\mathrm{MN}}(\boldsymbol{\sigma}) = \underbrace{\mathrm{tr}(\boldsymbol{\sigma})\,\mathrm{tr}(\boldsymbol{\sigma}^{-1}) - 9}_{H(\boldsymbol{\sigma})} - \underbrace{8\tan^2[\varphi]}_{H_{\max}(\varphi)}. \tag{7}$$

Therefore, a density-dependent friction angle φ is used:

$$\varphi = \varphi_c + \begin{cases}(\varphi_d - \varphi_c)\frac{e_c(P)-e}{e_c(P)-e_d(P)} & \text{for } e < e_c(P)\\ (\varphi_i - \varphi_c)\frac{e-e_c(P)}{e_i(P)-e_c(P)} & \text{for } e > e_c(P)\end{cases}. \tag{8}$$

The degree of nonlinearity Y reads

$$Y(x) = A_Y \exp\left(\frac{-1}{B_Y x^{n_Y} + C_Y}\right) \tag{9}$$

with

$$x = \frac{H(\boldsymbol{\sigma})}{H_{\max}(\varphi)} \quad \text{and} \quad A_Y = \exp\left(\frac{1}{B_Y + C_Y}\right) \tag{10}$$

using the parameters B_Y, C_Y, and n_Y and the friction angles φ_c, φ_d, and φ_i.

The hypoplastic equivalent flow rule $\boldsymbol{m}$ describes the direction of the irreversible deformations. An improvement compared to earlier NHP versions concerns the modeling of the phase transformation, which depicts the change from contractive to dilative soil response. As documented, for example, by [35, 36], the phase transformation is influenced by the current soil density. To consider this observation in the constitutive model, the hypoplastic equivalent flow rule $\boldsymbol{m}$, which is for some special stress states explicitly defined as

$$m_{ij} = \begin{cases} m^a_{ij} = \left[\delta_{ij}\sigma^{-1}_{kk} - \sigma_{kk}\sigma^{-2}_{ij}\right]^{\rightarrow} & \text{if } \frac{H(\boldsymbol{\sigma})}{H_{\max}(\varphi_a)} \geq 1\\ m^c_{ij} = \left(\left[\delta_{ij}\sigma^{-1}_{kk} - \sigma_{kk}\sigma^{-2}_{ij}\right]^{*}\right)^{\rightarrow} & \text{if } \frac{H(\boldsymbol{\sigma})}{H_{\max}(\varphi_{\mathrm{PT}})} = 1\\ m^i_{ij} = -\left(\delta_{ij}\right)^{\rightarrow} & \text{if } H = 0\end{cases}, \tag{11}$$

includes a phase transformation friction angle

$$\varphi_{\mathrm{PT}} = \varphi_c + (\varphi_i - \varphi_c)\left\langle\frac{e_c(P) - e}{e_c(P) - e_d(P)}\right\rangle. \tag{12}$$

In the densest state ($e = e_d(P)$), the phase transformation friction angle is small ($\varphi_{\mathrm{PT}} = \varphi_i$), whereas in the critical state ($e = e_c(P)$), φ_{PT} equals $\varphi_c > \varphi_i$. The interpolation between these in Equation (11) explicitly defined cases is formulated using the parameters n_1 and n_2:

$$\begin{aligned}\boldsymbol{m} &= \left[y\boldsymbol{m}^c + (1-y)\boldsymbol{m}^i\right]^{\rightarrow} \quad \text{for } y = \left(\frac{H(\boldsymbol{\sigma})}{H_{\max}(\varphi_{\mathrm{PT}})}\right)^{n_1}\\ \boldsymbol{m} &= \left[y\boldsymbol{m}^a + (1-y)\boldsymbol{m}^c\right]^{\rightarrow} \quad \text{for } y = \left(\frac{H(\boldsymbol{\sigma}) - H_{\max}(\varphi_{\mathrm{PT}})}{H_{\max}(\varphi_a) - H_{\max}(\varphi_{\mathrm{PT}})}\right)^{n_2}\end{aligned}. \tag{13}$$

It is well known that the current anisotropic fabric (anisotropic microstructure) of a soil sample significantly influences its overall macroscopic behavior [35, 37–39]. In addition to the effective Cauchy-stress $\boldsymbol{\sigma}$ and the void ratio e, an evolving deviatoric fabric tensor $\boldsymbol{z}$ is therefore included as state variable in the NHP. Using this state variable, the NHP can qualitatively account for the effect of an anisotropic microstructure, such as the effects of sample preparation techniques [36, 39] and the influence of the direction of the major principal stress relative to the sedimentation axis [38, 40–42].

An additional nonlinearity with the intensity

$$Y_z = \omega(z_{\max} - \boldsymbol{z} : \vec{\boldsymbol{\varepsilon}}) \tag{14}$$

and the direction $\boldsymbol{m}^z = \vec{\boldsymbol{\sigma}}$ is, therefore, introduced. For isotropic stress states, Equation (14) leads to an additional contractancy. Note that Equation (14) differs from earlier NHP versions to model a smooth transition for the intensity of the fabric effect as a function of the applied strain rate direction. The larger the difference between the direction of the fabric tensor $\boldsymbol{z}$ and the

direction of the applied strain rate $\vec{\dot{\varepsilon}}$, the larger becomes Y_z. The greatest influence of the fabric on the material behavior occurs for a fully mobilized fabric tensor with its asymptotic value $\|\boldsymbol{z}\| = z_{\max}$ due to a 180° reversal of the loading direction. In this case, $Y_z = 2\omega z_{\max}$ applies.

The intensity of the additional contractancy due to fabric effects is pressure-dependent, modeled using the function

$$\omega = \frac{P_z}{z_{\max}(100\,P_0 + P)}\, f_{ac}(e) \tag{15}$$

with the parameter P_z and the reference pressure P_0. The function $f_{ac}(e)$ deactivates the additional contractancy for dense states ($e < e_d(P)$).

Inadmissible dense states with $e \ll e_d(P)$ are avoided in the NHP by the term $\boldsymbol{m}^d Y_d \|\dot{\boldsymbol{\varepsilon}}\|$ in Equation (2).

The fabric tensor $\boldsymbol{z}$ can be interpreted as rolling of grains [24, 27, 43, 44]. The underlying hypothesis assumes that individual grains can roll over each other due to a monotonic shearing. Due to a reversal in loading direction, the grains can roll back, which induces the described pronounced additional contractancy. The evolution equation of the fabric tensor reads

$$\dot{\boldsymbol{z}} = A_z \left(\dot{\boldsymbol{\varepsilon}}^{\diamond} - \vec{\boldsymbol{z}} \left(\frac{\|\boldsymbol{z}\|}{z_{\max}} \right)^{\beta_z} \|\dot{\boldsymbol{\varepsilon}}^{\diamond}\| \right) \left(\alpha_z + \left(\frac{\|\boldsymbol{z}\|}{z_{\max}} \right)^{n_z} \right) \tag{16}$$

with

$$\dot{\boldsymbol{\varepsilon}}^{\diamond} \overset{\text{def}}{=} \left(\frac{\dot{\varepsilon}_Q^2}{\dot{\varepsilon}_Q^2 + \dot{\varepsilon}_P^2} \right)^{10} \dot{\boldsymbol{\varepsilon}}^{*} \tag{17}$$

and the parameters β_z, α_z, and n_z. $\boldsymbol{z}$ only evolves due to a deviatoric strain rate, which is scaled by the proportion of the deviatoric to the total strain rate. A sufficiently long monotonic shearing results in an asymptotic value of $\boldsymbol{z}$ with $\|\boldsymbol{z}\| = z_{\max}$ and $\vec{\boldsymbol{z}} \propto \vec{\dot{\boldsymbol{\varepsilon}}}^{*}$. Small deviatoric strain cycles reduce the fabric tensor to $\|\boldsymbol{z}\| = 0$ [43, 44], which leads to a hyperelastic stiffness $\overline{\mathsf{E}}$.

The fabric tensor $\boldsymbol{z}$ and the interpretation of the rolling of grains in NHP are reminiscent of the fabric-dilatancy internal variable $\boldsymbol{z}$ from the Sanisand model [45]. However, it should be noted that the fabric tensor $\boldsymbol{z}$ in the NHP does not only evolve during dilative deformations, although Equation (16) should ensure that the fabric evolution in the case of $\|\boldsymbol{z}\| \approx 0$ occurs significantly slower than in the case of $\|\boldsymbol{z}\| \gg 0$ [24].

As a simplification, an additional parameter u_z is added to control the overall evolution of the fabric tensor $\boldsymbol{z}$ in the factor A_z in Equation (16):

$$A_z = \frac{F_e\, u_z}{c\,(2 - n - \alpha)(P/P_0)^{1-n}}\,. \tag{18}$$

In the NHP version of [24], u_z was not specified as a separate parameter. Instead, a constant in Equation (18) was derived based on an intended fabric erasure caused by deformation that starts at the critical state line and ends at an isotropic stress state. For practical reasons, a direct specification of u_z as a constitutive parameter was found to be more suitable as this parameter u_z directly controls the overall fabric evolution.

These novelties results overall in 29 constitutive parameters (instead of 27 in [24]) for the NHP (without small strain stiffness extension). However, as discussed in Section 5, only 11 of them need to be calibrated practically. For most granular materials, default values can be assigned to the remaining ones.

Similar to other hypoplastic models, the standalone NHP formulation cannot adequately reproduce the soil behavior due to cyclic loading. Therefore, a simple approach based on paraelasticity, similar to [46, 47], for considering small strain effects was coupled in [24] with the NHP. This so-called last-reversal approach needs only one additional parameter. A scalar factor k was introduced to scale the stiffness according to the distance in the strain space of the current strain state from the strain at the last reversal of the direction of loading. This approach works effectively for element test simulations considering only 180° loading direction reversals. However, due to "jumps" of the corresponding state variable, the approach seems to be problematic for simulations of complex boundary value problems (BVPs) and for general loading conditions [48]. To overcome this drawback, the NHP formulation is coupled in the following with the recently published GIS [5] concept.

Note, therefore, that Equation (2) can be formulated in terms of the extended generalized hypoplastic (Equation 1) by setting $S = Y$ and $C = 1$ with $\boldsymbol{f}(\dot{\boldsymbol{\varepsilon}}, \boldsymbol{\alpha}) \neq \boldsymbol{0}$.

3 | Generalized Intergranular Strain (GIS) Concept

The generalized intergranular strain (GIS) concept [5] is an extension to constitutive models to consider the effects due to small strains and cyclic loading. It is developed based on the original well-known intergranular strain (IS) concept [19]. However, the GIS approach exhibits some advantages over the IS formulation, some of which are unique to GIS and some of which have been taken over from other IS extensions. These include (a) a prevented overshooting, (b) an adequate modeling of nonlinear accumulation further called cyclic preloading (CP) effects as introduced in the intergranular strain improvement (ISI) [29], and (c) a straightforward coupling with different base constitutive models. The state variable of the intergranular strain $\boldsymbol{h}$ memorizes the recent strain history. Its evolution can be expressed using [19]

$$\dot{\boldsymbol{h}} = \begin{cases} (\mathsf{I} - \vec{\boldsymbol{h}}\vec{\boldsymbol{h}}\rho^{\beta_r}) : \dot{\boldsymbol{\varepsilon}} & \text{if } \vec{\boldsymbol{h}} : \dot{\boldsymbol{\varepsilon}} > 0 \\ \dot{\boldsymbol{\varepsilon}} & \text{if } \vec{\boldsymbol{h}} : \dot{\boldsymbol{\varepsilon}} \leq 0 \end{cases} \tag{19}$$

with the direction of the IS defined as

$$\vec{\boldsymbol{h}} = \begin{cases} \frac{\boldsymbol{h}}{\|\boldsymbol{h}\|} & \text{if } \boldsymbol{h} \neq \boldsymbol{0} \\ \boldsymbol{0} & \text{if } \boldsymbol{h} = \boldsymbol{0} \end{cases} \tag{20}$$

and the current mobilization of the IS

$$\rho = \frac{\|\boldsymbol{h}\|}{R} \,. \tag{21}$$

The parameter R specifies the so-called elastic range and β_r controls the increase of $\boldsymbol{h}$. Due to sufficiently large monotonic deformation, $\dot{\boldsymbol{h}} = \boldsymbol{0}$ is asymptotically reached at a fully mobilized IS ($\rho = 1$).

In the GIS concept, a scalar factor k is introduced as follows:

$$k = [\rho^{\chi_R} m_T + (1 - \rho^{\chi_R}) m_R] + \begin{cases} \rho^{\chi_R}(1 - m_T)\vec{\boldsymbol{h}} : \vec{\hat{\boldsymbol{\varepsilon}}} & \text{if } \vec{\boldsymbol{h}} : \vec{\hat{\boldsymbol{\varepsilon}}} > 0 \\ -\rho^{\chi_R}(m_R - m_T)\vec{\boldsymbol{h}} : \vec{\hat{\boldsymbol{\varepsilon}}} & \text{if } \vec{\boldsymbol{h}} : \vec{\hat{\boldsymbol{\varepsilon}}} \leq 0 \end{cases} . \tag{22}$$

Equation (22) represents an interpolation for the factor k depending on the strain rate direction $\vec{\hat{\boldsymbol{\varepsilon}}}$ and the current IS $\boldsymbol{h}$. The parameters R, m_R, m_T, and χ_R (χ_R is renamed compared to the original IS concept) control this interpolation between the maximum value of $k = m_R$ and the minimum value of $k = 1$. Four special cases can be highlighted as follows [5]:

- $k = 1$ and $\rho = 1$ is reached asymptotically due to a sufficient large monotonic deformation.
- $k = m_R$ holds for a 180° loading direction reversal in the case of fully mobilized IS ($\rho = 1$).
- $k = m_T$ holds for a 90° loading direction reversal in the case of fully mobilized IS ($\rho = 1$).
- $k = m_R$ holds for $\rho = 0$, independent of the applied strain rate.

The factor k can be used for (a) scaling of the stiffness and (b) reducing irreversible deformations of the base constitutive model within the small strain range. For a hypoplastic base constitutive model formulated according to Equation (1), the GIS extension results in

$$\mathring{\boldsymbol{\sigma}} = k\, \mathsf{E} : \left(\dot{\boldsymbol{\varepsilon}} - \boldsymbol{m}\, C\, S^{(k^\gamma)}\, \|\dot{\boldsymbol{\varepsilon}}\| + \boldsymbol{f}(\dot{\boldsymbol{\varepsilon}}, \boldsymbol{\alpha}, k)\right) . \tag{23}$$

The exponent γ is expressed using

$$\gamma = \gamma_\chi \chi \tag{24}$$

with the parameter γ_χ. The function

$$\chi = \chi_0 + \Omega(\chi_{\max} - \chi_0) \tag{25}$$

can be defined, using further parameters χ_0 and $\chi_{\max}$ [29, 31]. The additional state variable Ω considers the CP effects and evolves towards unity ($\Omega \to 1$) in the case of cyclic loading with small strain cycles ($\rho \approx 0$). The CP vanishes to zero during sufficiently long monotonic loading paths or cyclic loading with large strain amplitudes. The evolution equation of the CP variable Ω reads as follows:

$$\dot{\Omega} = C_\Omega(1 - \rho^{\gamma_\Omega} - \Omega)\|\dot{\boldsymbol{\varepsilon}}\| \,. \tag{26}$$

Details about the CP variable can be found in [29, 49]. Note that Ω is mainly used to reproduce nonlinear accumulation behavior with the number of cycles N. The accumulation due to cyclic loading itself is governed by the base constitutive model and results from the irreversible strains or stresses after each individual cycle. A comparison of Ω with CP variables in accumulation models like the HCA model [50], which only capture accumulation trends, should be made with caution.

4 | NHP Coupled With GIS

For the NHP as base constitutive model in the GIS concept, Equation (23) can be rewritten as follows:

$$\mathring{\boldsymbol{\sigma}} = k\, \overline{\mathsf{E}} : \left(\dot{\boldsymbol{\varepsilon}} - \boldsymbol{m} Y^{(k^\gamma)} \|\dot{\boldsymbol{\varepsilon}}\| - \boldsymbol{m}^z Y_z{}^{(k^\gamma)} \|\dot{\boldsymbol{\varepsilon}}\| - \boldsymbol{m}^d Y_d \|\dot{\boldsymbol{\varepsilon}}\|\right) . \tag{27}$$

In Equation (27), the stiffness $\overline{\mathsf{E}}$ is increased for $k > 1$ while the irreversible deformations are reduced for $Y < 1$ using $Y^{(k^\gamma)}$. The condition $Y = 1$ is thus not affected. Consequently, the well-known problem of the overshooting of the limit condition is avoided within the NHP+GIS formulation. Irreversible deformations due to the additional contractancy induced by the fabric tensor $\boldsymbol{z}$ are similarly reduced using $Y_z{}^{(k^\gamma)}$. The factor A_z, defined in Equation (18), is derived using the stiffness [24] and therefore the scalar factor k must be considered also in the calculation of A_z:

$$A_z = k\, \frac{F_e\, u_z}{c\,(2 - n - \alpha)(P/P_0)^{1-n}} \,. \tag{28}$$

Numerical examples have shown that the term $\boldsymbol{m}^d Y_d \|\dot{\boldsymbol{\varepsilon}}\|$ preventing inadmissible dense states calculated using $Y_d = f(Y)$ should not be modified when coupling NHP with GIS.

In total, the coupled NHP+GIS model includes five state variables as follows:

- effective Cauchy-stress $\boldsymbol{\sigma}$,
- void ratio e,
- fabric/structure tensor $\boldsymbol{z}$,
- intergranular strain $\boldsymbol{h}$,
- cyclic preloading variable Ω.

Note that sufficiently long monotonic deformation results in $\dot{\boldsymbol{z}} = \boldsymbol{0}$, $\dot{\Omega} = 0$, and $\dot{\boldsymbol{h}} = \boldsymbol{0}$ and these state variables will tend to asymptotic values. In the following, the parameter calibration of NHP+GIS is discussed and the model's performance is demonstrated using element test simulations and finite element analyses.

5 | Parameter Calibration

The coupled constitutive model NHP+GIS contains a total of 39 constitutive parameters. 29 of the overall parameters relate to the base NHP model and 10 to the GIS extension. The latter can be subdivided into 5 parameters overtaken from the original IS concept and further 5 parameters to consider CP effects. Despite a large number of parameters, the parameter calibration of the NHP+GIS is straightforward as described below.

TABLE 1 | Proposed 18 advanced parameters (can be used for any granular material without further calibration) of NHP.

P_0 [kPa]	n [—]	α [—]	n_1 [—]	n_2 [—]	β_L [°]	β_D [°]	n_L [—]	B_Y [—]	C_Y [—]	n_Y [—]	a_z [—]	n_z [—]	β_z [—]	u_z [—]	$z_{\max}$ [—]	k_d [—]	k_e [—]
1	0.6	0.1	0.22	0.9	30	−15	0.1	12	0.35	1.1	0.01	2	0.15	0.4	0.05	200	1.5

5.1 | Calibration of the NHP Parameters

It turns out that for the base model of the NHP 18 of the 29 mentioned parameters can be treated as advanced parameters or "constants." They can be set to a default value and do not need to be calibrated for different materials. The default values of these quantities are summarized in Table 1. Each parameter is discussed in detail in [24]. The proposed values of the advanced parameters have changed slightly compared to [24] due to intensive element test simulations and their comparison with experimental data.

Therefore, only 11 parameters of the NHP need to be calibrated by practitioner. Furthermore, the calibration procedure is quite similar to that proposed for earlier hypoplastic models [2, 51, 52].

The granular hardness h_s, the exponent n_B, and the limit void ratios at zero mean effective pressure e_{d0}, e_{c0}, and e_{i0} correspond to the well-known compression curve after Bauer [10]. The parameters h_s and n_B control the shape of the compression curve and can be calibrated using simulations of an oedometric compression test on a loose sample [2, 51, 52]. The limit void ratios at zero pressure can be obtained from laboratory tests to determine the minimum void ratio $e_{\min}$ (densest state) and the maximum void ratio $e_{\max}$ (loosest state) [2, 51, 52]:

$$e_{d0} \approx e_{\min}\,, \quad e_{c0} \approx e_{\max}\,, \quad e_{i0} \approx 1.2\, e_{\max}\,. \tag{29}$$

The parameter c controls the magnitude of the hyperelastic stiffness and can be calibrated using the stress–strain curve of a drained triaxial test on a loose sample. In a first approximation, $c \approx 0.001$ can be assumed.

The critical friction angle φ_c can be derived either from angle of response tests or triaxial tests [2, 51, 52]. It is further proposed to assume

$$\varphi_i \approx 0.750 \text{ to } .9\,\varphi_c \quad \text{and} \quad \varphi_d \approx \varphi_a \approx 1.5\,\varphi_c \tag{30}$$

for the remaining friction angles φ_i, φ_d, and φ_a. Slight deviations of these proposed ratios can permit a more detailed parameter calibration. The same applies to the remaining 18 advanced parameters with the proposed default values from Table 1.

The parameter P_z controls the intensity of the fabric effects and their pressure dependency according to Equation (15). A practical calibration can be performed using undrained monotonic triaxial compression and extension tests on loose samples prepared with the same sample preparation method and sedimentation direction. Such samples exhibit significantly more contractive behavior in triaxial extension tests than in triaxial compression tests. This behavior can be reproduced by appropriately choosing P_z and by properly initializing the fabric tensor, as described in Section 6 and shown in Figure 6. A larger P_z results in more pronounced anisotropic effects. The fabric effects can be deactivated by setting $P_z = 0$.

5.2 | Calibration of the GIS Parameters

For the calibration of the 10 GIS parameters, it can be distinguished between the 5 original IS parameters and the 5 additional GIS parameters for considering CP effects. The original IS concept [19] is widely used and details on the parameter calibration can be found in the literature [2, 19]. As a first approximation, the corresponding 5 parameters can be adopted directly into the GIS concept.

The parameter R specifies the size of the elastic range. In practice, this range can be determined using resonant column tests or tests with local strain measurements. The multipliers m_R and m_T represent the stiffness increase factor k due to a change of loading direction of 180° and 90° respectively. Generally, $m_R > m_T > 1$ applies. The remaining parameters β_R and χ_R control the stiffness degradation with increasing strain amplitude and can be determined using the same tests used to determine the elastic range [19].

The 5 additional GIS parameters are discussed in detail in [29]. It is recommended to use a cyclic undrained triaxial test with a prescribed stress amplitude q^{ampl} for parameter calibration. The s-shaped accumulation curve of the pore fluid pressure (corresponds to the accumulation of the decrease of the mean effective stress) as a function of the number of cycles is considered. First, the parameter γ_χ needs to be calibrated without taking the state variable Ω into account such that a faster pore fluid pressure accumulation is achieved by the simulations compared to the experiment. Based on this γ_χ, the remaining four parameters can then be calibrated.

The parameter χ_0 controls the accumulation rate within the first cycles. The greater χ_0, the weaker the build-up of pore fluid pressure within the first cycles. Note that in the NHP+GIS model, an intensified reduction of the mean effective pressure within the first cycles can also result from a properly initialized fabric tensor $\mathbf{z}$. This must be taken into account when calibrating the GIS parameters and primarily for the calibration of χ_0. The parameter $\chi_{\max}$ controls the accumulation rate after a large number of cycles with a small strain amplitude. The greater $\chi_{\max}$, the lower the accumulation rate. The transition between the fast accumulation at the beginning of the test and the slower accumulation after a larger number of cycles can be controlled by C_Ω. The greater C_Ω, the faster the accumulation rate is reduced. The parameter γ_Ω has a similar effect. For the NHP+GIS $0 < \gamma_\chi < 0.5$, $\chi_0 \approx 1$, $\chi_{\max} > \chi_0$, $20 < C_\Omega < 90$ and $\gamma_\Omega \approx 1$ applies approximately.

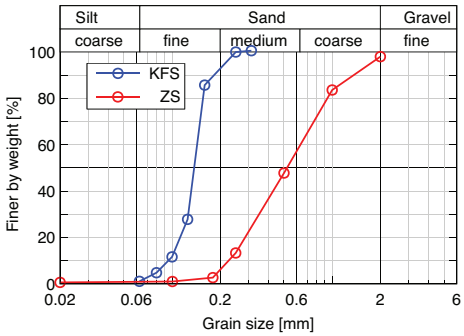

FIGURE 1 | Grain size distribution of KFS and ZS.

TABLE 2 | NHP parameters for Karlsruhe fine sand (KFS) and Zbraslav sand (ZS).

	c [—]	h_s [kPa]	n_B [—]	e_{i0} [—]	e_{c0} [—]	e_{d0} [—]	φ_i [°]	φ_c [°]	φ_d [°]	φ_a [°]	P_z [kPa]
KFS	0.001	$4 \cdot 10^6$	0.27	1.212	1.054	0.677	25	33.1	50	50	40
ZS	0.001	111746	0.346	1.027	0.893	0.52	31	34	49	49	20

TABLE 3 | GIS parameters for the coupled NHP+GIS model for Karlsruhe fine sand (KFS) and Zbraslav sand (ZS).

	R [—]	m_R [—]	m_T [—]	β_R [—]	χ_R [—]	γ_χ [—]	χ_0 [—]	$\chi_{\max}$ [—]	C_Ω [—]	γ_Ω [—]
KFS	10^{-4}	5	2	0.5	6.0	0.28	1.45	2.73	50	1.0
ZS	10^{-4}	5	2.5	0.5	6	0.31	1.09	2.214	41	1.0

Although the GIS parameters can be calibrated using cyclic undrained triaxial tests, additional cyclic tests such as cyclic oedometric tests including un- and reloading can also be used to improve the parameter calibration. Finally, it should be noted that the GIS and the NHP parameters obviously influence each other and thus, after the calibration of the GIS parameters based on cyclic tests, the NHP parameters obtained from monotonic tests should perhaps be slightly adjusted.

5.3 | Calibrated Parameters for Two Sands

The NHP+GIS model has been calibrated for Karlsruhe fine sand (KFS) and Zbraslav sand (ZS). The grain size distributions of both quartz sands are shown in Figure 1. Details about KFS can be found in [35, 36, 53] and for ZS in [49, 54, 55, 56]. The calibrated NHP parameters are given in Table 2 and the GIS parameters are given in Table 3. The NHP+GIS parameters are based on the HP+IS parameters for KFS from [35] and for ZS from [49]. These parameter sets were adopted and supplemented with the additional parameters for the NHP+GIS model.

6 | Element Tests: Simulations vs. Experimental Data

Element test simulations using the NHP+GIS are presented and compared with experimental data from both KFS and ZS in the following. The experimental data were taken from [36, 53–56] and can be downloaded from the internet [57, 58]. The open-source code *IncrementalDriver* [59] is used for the simulations and the NHP+GIS is implemented using an *Abaqus* subroutine *umat.for*.

The initialization of the state variables is of high relevance for the comparison of simulations with test data. The effective initial stress state $\boldsymbol{\sigma}_0$ and the initial void ratio e_0 can be measured in the tests and initialized accordingly. The initialization of additional state variables is, however, not straightforward and challenging since they cannot be measured directly in conventional experiments equipped with conventional instrumentation. For triaxial tests with a hydrostatic initial stress state, one could initialize the IS fully mobilized with $\boldsymbol{h}_0 = -R/\sqrt{3}\boldsymbol{\delta}$ due to the previous isotropic compression. However, even a small cyclic loading, which can be induced for example by small vibrations of the experimental device, would rapidly decrease the IS. These uncertainties are not quantifiable. In the subsequent simulations, the IS is, therefore, initialized to $\boldsymbol{h}_0 = -0.9R/\sqrt{3}\boldsymbol{\delta}$. In the oedometric tests, the IS is initialized completely mobilized with $h_a = -R$ due to the sedimentation in the axial direction. As there exists no pronounced CP in the considered experiments, $\Omega_0 = 0$ is initialized in all simulations.

Experimental studies have shown that the method of sample preparation significantly influences the mechanical behavior of soil [36, 60–62]. The observed differences can be attributed to the sample's current fabric, which depends mainly on the preparation method. Different sample preparations can be considered by a different value of the initial fabric tensor $\boldsymbol{z}_0$. For the initialization of the fabric tensor $\boldsymbol{z}_0$ in the subsequent element test simulations, a transverse isotropy in correspondence to the sedimentation direction aligned with the x_1 axis (axial direction) can be assumed:

$$\boldsymbol{z}_0 = \|\boldsymbol{z}_0\| \begin{bmatrix} -2/\sqrt{6} & 0 & 0 \\ 0 & 1/\sqrt{6} & 0 \\ 0 & 0 & 1/\sqrt{6} \end{bmatrix}. \tag{31}$$

Thus, only the norm $\|\boldsymbol{z}_0\|$ is unknown. The following triaxial tests on KFS are prepared using dry air pluviation (AP) or moist tamping (MT) [36, 54] and the samples on ZS are prepared by dry deposition in the loosest state with subsequent compaction [55]. The resulting different initial fabric is considered qualitatively by initializing $\|\boldsymbol{z}_0\| = 0.4 z_{\max}$ for AP samples and $\|\boldsymbol{z}_0\| = z_{\max}$ for samples using MT or dry deposition in the loosest state with subsequent compaction[2]. Note that only MT samples are labeled in the figures below. KFS samples without mentioning the preparation method are AP samples. If the initialization differs from the above-mentioned values, it is indicated and reasoned.

In the future, micro-mechanical investigations, for example, using x-ray tomography [63], could provide more in-depth information about the fabric and its evolution.

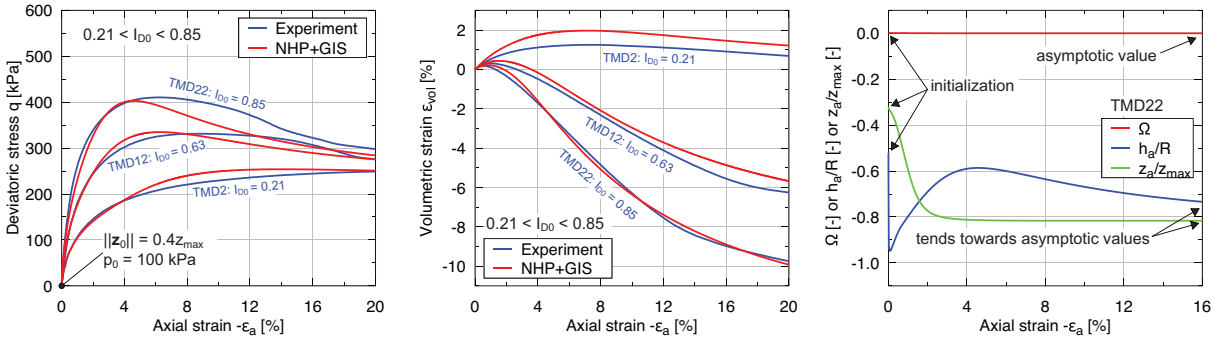

FIGURE 2 | Experimental results [36] versus simulations with NHP+GIS for monotonic drained triaxial compression tests on KFS for samples with different initial densities: (a) deviatoric stress q, (b) volumetric strain ε_{vol}, and (c) state variables Ω, h_a, and z_a as a function of the axial strain ε_a.

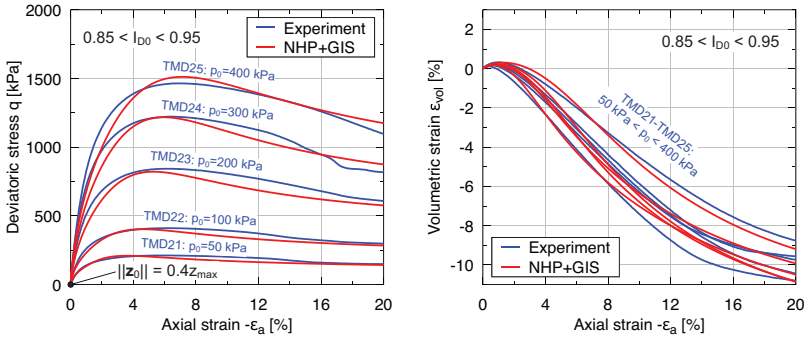

FIGURE 3 | Experimental results [36] versus simulations with NHP+GIS for monotonic drained triaxial compression tests on dense KFS samples with varying mean effective pressure: (a) deviatoric stress q and (b) volumetric strain ε_{vol} as a function of the axial strain ε_a.

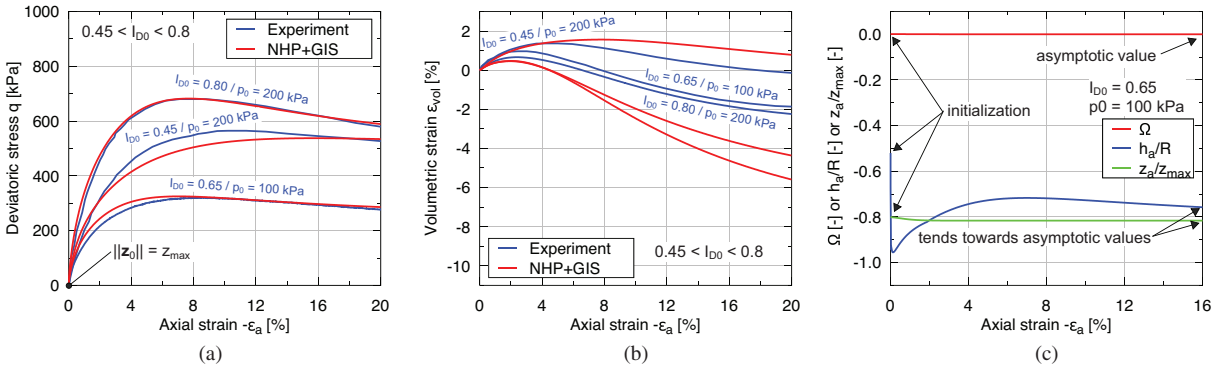

FIGURE 4 | Experimental results [49] ($p_0 = 100$ kPa), [53] ($p_0 = 200$ kPa) versus simulation with NHP+GIS for monotonic drained triaxial compression tests on ZS: (a) deviatoric stress q; (b) volumetric strain ε_{vol}; and (c) state variables Ω, h_a, and z_a as a function of the axial strain ε_a.

6.1 | Monotonic Drained Triaxial Tests

Monotonic drained triaxial tests on KFS are shown in Figure 2 for different initial densities and in Figure 3 for dense samples with varying initial mean effective pressure. Figure 4 presents drained triaxial compression tests on ZS samples with varying initial density and mean effective pressure.

The stress–strain curves (deviatoric stress q as a function of the axial strain ε_a) in Figures 2a, 3a, and 4a show a remarkably good agreement between simulations and experiments. The peak strength of dense samples, the asymptotic deviatoric stress at large strain as well as the density-dependent stiffness can be reproduced. The volumetric strain ε_{vol} as a function of the axial strain ε_a can also be modeled well, see Figures 2b, 3b, and 4b. Both, the initial contractancy and the subsequent pronounced dilatancy of dense samples are reproduced. As demonstrated in Figure 3, the soil behavior due to a drained triaxial compression can be reproduced by the NHP+GIS across a wide range of mean effective pressures, whereby an increase in mean effective

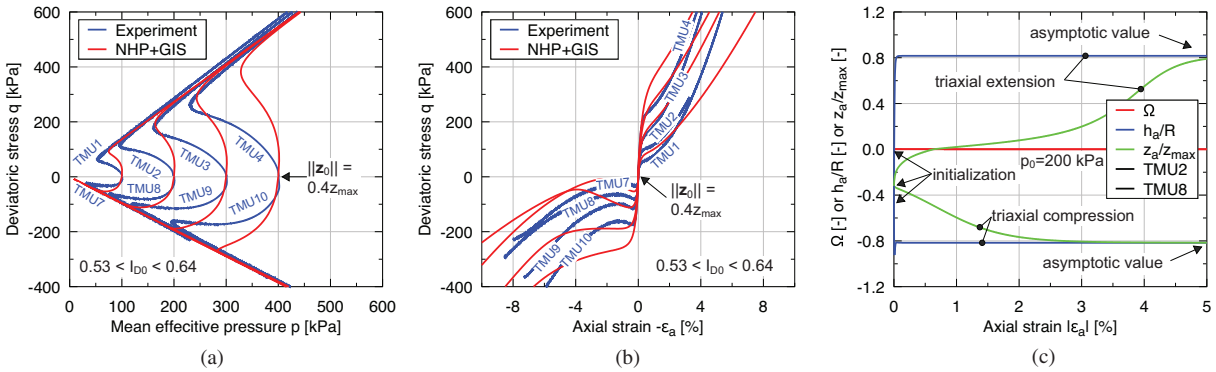

FIGURE 5 | Experimental results [36] versus simulations with NHP+GIS for monotonic undrained triaxial compression and extension tests on KFS with varying initial mean effective pressure: (a) effective stress path in the pq diagram, (b) deviatoric stress q, and (c) state variables Ω, h_a, and z_a as a function of axial strain ε_a.

pressure leads to an increase in the deviatoric stress reached within the test. In addition to the reliable modeling of the dilatancy of the dense sample, it is worth emphasizing that the strain upon reaching the peak stress is well reproduced. Note that both effects cannot be modeled accurately using HP+IS.

Figures 2c and 4c show the evolution of the additional state variables (Ω, $\boldsymbol{h}$ and $\boldsymbol{z}$) during two of the shown drained triaxial compression tests (KFS and ZS). No relevant change of the CP variable Ω occurs during the monotonic deformation and $\Omega_0 = 0$ is reached asymptotically. If the CP was to be initialized as $\Omega_0 \neq 0$, a monotonic deformation would erase the CP. Pronounced changes in the fabric tensor $\boldsymbol{z}$ can be seen for the KFS sample, whereby the fabric in the ZS changes only slightly due to the already initialized asymptotic value. The IS $\boldsymbol{h}$ is initialized in both samples identically. However, the considered experiments exhibit, mainly due to different initial densities, different strain paths, and the evolution of $\boldsymbol{h}$, therefore, differs within both simulations. A monotonic drained triaxial test leads asymptotically to a volume-constant proportional strain path (critical state). This explains the asymptotic values of all state variables and the same direction of $\boldsymbol{z}$ and $\boldsymbol{h}$ in this specific asymptotic state.

6.2 | Monotonic Undrained Triaxial Tests

The results of monotonic undrained triaxial compression and extension tests on KFS are shown for medium-dense samples with different initial mean effective pressures in Figure 5 and for different initial densities in Figure 6.

The dense and medium-dense samples undergo a phase transformation from the initial contractive to a dilative behavior during the test, indicated by a subsequent increase in the mean effective pressure. The phase transformation line, that is, the mobilized friction angle at which the phase transformation occurs, is density-dependent and decreases with increasing density [36]. These effects can be reproduced by the NHP+GIS in the compression test.

A slight deviation in the effective stress path in the pq diagram between the simulations and the experiments can be seen in Figures 5a and 6a. The simulations reveal a less pronounced reduction in the mean effective pressure, that is, a lack of contractive behavior, at the beginning of the tests. This shortcoming can be attributed to the base model NHP and does not result from the GIS extension. The simulations could be improved by modifying (advanced) parameters for the degree of nonlinearity Y, the equivalent hypoplastic flow rule $\boldsymbol{m}$, or the influence of the fabric $\boldsymbol{z}$. However, for a general calibration of the constitutive parameters for a wide range of different tests, no such optimization was conducted as part of this work.

The deviatoric stress q as a function of the axial strain ε_a, as shown in Figures 5b and 6b, demonstrates a reasonable modeling of the soil stiffness. Especially, the increased stiffness at small stress ratios at the beginning of the test and the significantly reduced stiffness at large stress ratios are reproduced.

It should be emphasized that the NHP+GIS is qualitatively suitable to model the anisotropic soil behavior, which is indicated in the discussed tests by the significantly more pronounced stress relaxation and the softer behavior of the sample during triaxial extension compared to triaxial compression. The constitutive model provides this effect due to the initialization of the fabric tensor according to sedimentation in the vertical direction.

The evolution of the state variables Ω, $\boldsymbol{h}$, and $\boldsymbol{z}$ is shown for a triaxial compression and a triaxial extension test in Figure 5c. The same dependencies as already described for the monotonic drained triaxial test can be seen. The asymptotic values in extension and compression have opposite signs. Moreover, it is also obvious that due to the initialization of $\boldsymbol{z}$, more deformation is required to reach the asymptotic value in triaxial extension than in compression. Thus, the fabric influence is increased in extension direction and the anisotropic soil behavior can be modeled.

Three monotonic undrained triaxial compression tests on very loose KFS samples with different initial mean effective pressures prepared using the MT technique are shown in Figure 7. Due to the loose packing ($e_0 > e_c(p_0)$), a significant reduction in the mean effective pressure (contraction) is observed in all tests due to the applied shearing. Finally, a static soil liquefaction ($p = q = 0$)

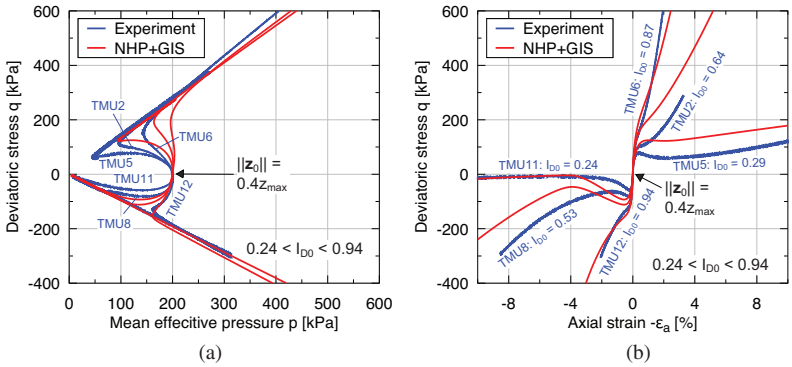

FIGURE 6 | Experimental results [36] versus simulations with NHP+GIS for monotonic undrained triaxial compression and extension tests on KFS with varying initial void ratio: (a) effective stress path in the pq diagram and (b) deviatoric stress q as a function of axial strain ε_a.

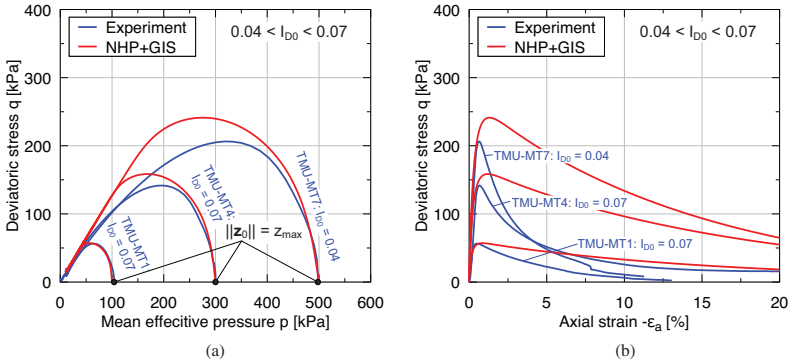

FIGURE 7 | Experimental results [36] versus simulations with NHP+GIS for monotonic undrained triaxial compression tests with varying initial mean effective pressure on very loose KFS samples (MT preparation): (a) effective stress path in the pq diagram and (b) deviatoric stress q as a function of axial strain ε_a.

occurs. The different initial pressures only cause a temporarily higher deviatoric stress, but do not affect the asymptotically reached static soil liquefaction.

The NHP+GIS can reproduce this soil behavior qualitatively, although the softening after the peak stress occurs much faster in the experiments than in the simulations. Hence, the simulations do not exhibit a complete static liquefaction at the considered strains.

Experiments on samples prepared using different sample preparation methods (air pluviation (AP) and moist tamping (MT)) are shown in Figure 8. The influence of the sample preparation on the subsequent mechanical behavior of the sample becomes obvious and is demonstrated for different initial effective pressures. The AP samples generally behave more contractive and less stiff than the MT samples, which can be seen in the effective stress path in Figure 8a as well as in the stress–strain curve in Figure 8b. As already mentioned above, the initial fabric is initialized for the MT samples to $\|\mathbf{z}_0\| = z_{\max}$. In contrast to the other simulations, $\|\mathbf{z}_0\| = 0$ is initialized for the loose AP samples considered here to clarify the effects. The simulations performed at different mean effective pressures show that the model can reproduce the general difference between the two preparation methods qualitatively. However, some noticeable differences between the simulations and the experiments can be observed. The simulated AP samples behave generally less contractive than the tests while the simulated MT samples behave qualitatively too contractive than the experiments. The simulations predict notably smaller deviatoric stress levels than the experiments for both, the AP and the MP samples.

Results of monotonic undrained triaxial tests on ZS on medium dense samples with different mean initial effective pressures are shown in Figure 9 and the influence of different densities is shown in Figure 10. First of all, it can be observed that the experiments using ZS show significantly less contractive behavior compared to the KFS. This may be due to the different preparation methods (i.e., the initial fabric), but can also, be attributed to the different material. The above-mentioned differences between the experimental data and the simulations for KFS do not apply to the results for ZS, and the data for ZS can be modeled quite accurately. Merely the simulations of the loose tests are a bit too contractive and too soft compared to the experiments. This small deviation could be caused by a small discrepancy in the calibrated compression curve of the limit void ratios. Thus, even better correlations between experiments and simulations could be achieved by slightly increasing the parameter e_{c0}. However, since this parameter was taken from [49], such an adjustment was avoided.

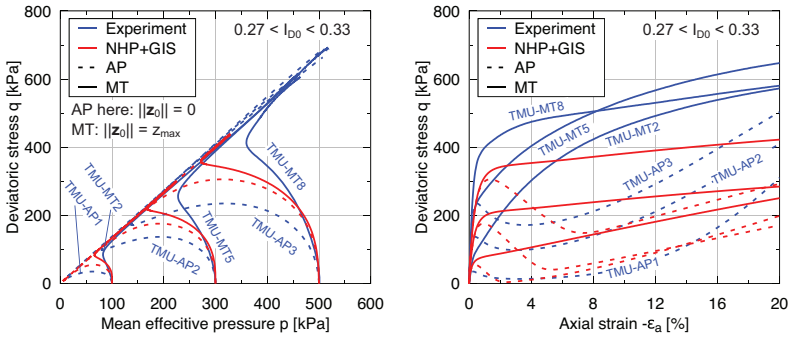

FIGURE 8 | Experimental results [36] versus simulations with NHP+GIS for monotonic undrained triaxial compression tests on loose KFS samples prepared using different sample preparation methods (AP and MT): (a) effective stress path in the pq diagram and (b) deviatoric stress q as a function of axial strain ε_a.

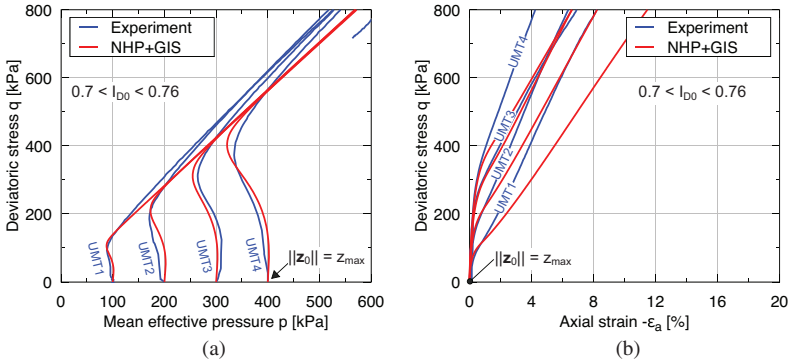

FIGURE 9 | Experimental results [56] versus simulations with NHP+GIS for monotonic undrained triaxial compression tests on ZS with varying initial mean effective pressure: (a) effective stress path in the pq diagram and (b) deviatoric stress q as a function of axial strain ε_a.

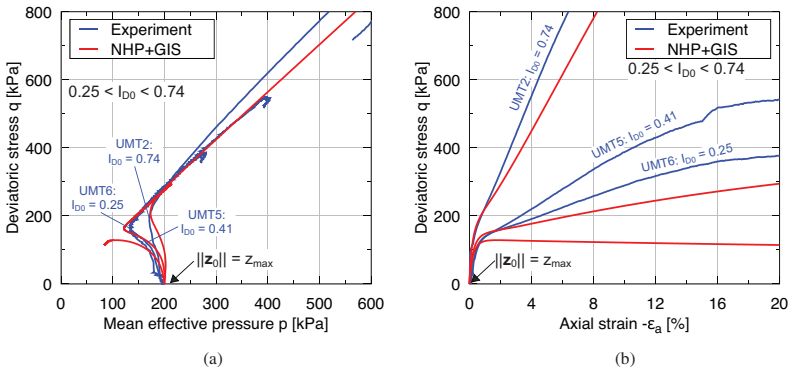

FIGURE 10 | Experimental results [56] versus simulations with NHP+GIS for monotonic undrained triaxial compression tests on ZS with varying initial void ratio: (a) effective stress path in the pq diagram and (b) deviatoric stress q as a function of axial strain ε_a.

6.3 | Oedometric Tests

Oedometric compression tests are considered subsequently. In these tests, the initial stress state cannot be measured in the experiments and an anisotropic effective initial stress state with $\sigma_{a0} = 1$ kPa and $\sigma_{r0} = K_0\sigma_{a0} = (1 - \sin\varphi_c)\sigma_{a0}$ is assumed. The initial IS is set to be fully mobilized in the axial direction with $h_{a0} = -R$ and $\rho = 1$. The fabric tensor is initialized with $\|\boldsymbol{z}_0\| = z_{\max}$ for KFS samples and $\|\boldsymbol{z}_0\| = 0$ for ZS samples to account for pronounced uncertainties at the beginning of a test at small stresses, as mentioned in [36]. To the best knowledge of the authors, there is a lack of experimental studies on the influence of the initial fabric for example due to different preparation methods on the results of oedometric compression tests.

The void ratio e as a function of the axial stress σ_a is shown in Figure 11 for tests on KFS and in Figure 12 for tests on ZS. Figures 11a and 12a present tests with a virgin loading and

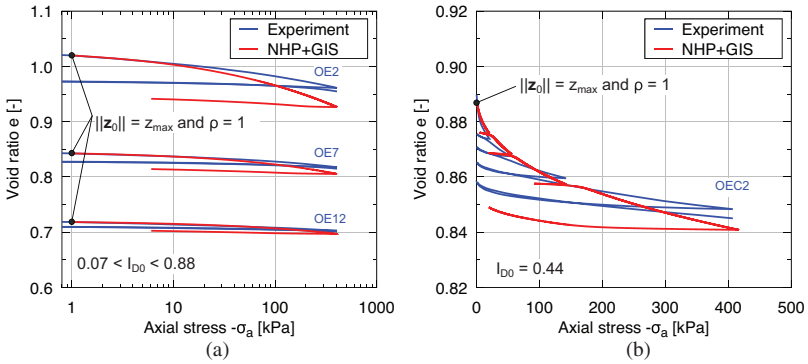

FIGURE 11 | Experimental results [36, 54] versus simulations with NHP+GIS for oedometric compression tests on KFS with varying initial density: void ratio e as a function of the axial stress σ_a for tests (a) with a virgin loading and unloading and (b) with four un- and reloading cycles.

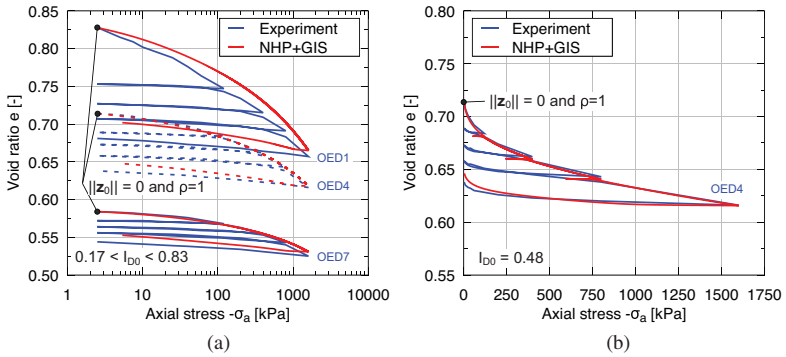

FIGURE 12 | Experimental results [56] versus simulations with NHP+GIS for oedometric compression tests on ZS with varying initial density: void ratio e as a function of the axial stress σ_a for tests (a) with a virgin loading and unloading and (b) with four un- and reloading cycles.

subsequent unloading for three different initial densities. Tests for an initial medium dense sample with four un- and reloading cycles are presented in Figures 11b and 12b.

The oedometric stiffness can be reproduced qualitatively well for both virgin loading and unloading across all considered densities and pressures. Solely, the stiffness due to the virgin loading of the loose KFS sample is slightly underestimated by the NHP +GIS.

As already mentioned in Section 4 and Equation (27), the NHP is coupled with the GIS concept by setting $S = Y$ and using the explicitly defined degree of nonlinearity Y. Using such a coupling, the overshooting of the limit stress state ($Y = 1$) due to an un- and reloading is effectively reduced. However, $Y = 1$ does not generally apply to all asymptotic states. All compressive proportional strain paths with an asymptotic mobilized friction angle of $\varphi_{\text{mob}} < \varphi_c$ (isotropic or oedometric compression for example) tend asymptotically to a degree of nonlinearity of $Y < 1.0$. Therefore, in the NHP+GIS, only the prevented overshooting of the limit stress state ($Y = 1$) can be expected, while there is still an overshooting issue of the oedometric or isotropic compression line due to unloading and reloading. Furthermore, as in the original IS concept, undershooting must be expected if the un- and reloading amplitude is too large. In Figures 11b and 12b, the unloading was, therefore, chosen such that neither undershooting nor overshooting occurs. The oedometric un- and reloading cycles can also be represented qualitatively. Note that the GIS parameters were not calibrated using the oedometric tests but instead using cyclic and undrained triaxial tests described in the next paragraph.

It should be mentioned that the overshooting of the entire asymptotic state boundary surface (ASBS) can be prevented in the GIS concept if the state mobilization S is formulated considering all asymptotic states. For example, the overshooting of the oedometric compression line is avoided in the HP+GIS formulation presented in [5].

6.4 | Undrained Cyclic Triaxial Tests With Prescribed Stress Amplitude

In cyclic undrained triaxial tests with a given symmetric amplitude of the deviatoric stress q^{ampl}, an accumulative decrease of the mean effective stress occurs due to the prevented contractancy after each loading direction change. In experiments with constant mean total pressure, the latter is associated with a buildup of the measured pore fluid pressure, which accumulates highly nonlinearly with the number of cycles.

Figure 13 presents a cyclic undrained triaxial test on KFS with a given stress amplitude of $q^{\text{ampl}} = 40$ kPa, while Figure 14 presents a test for ZS with a slightly larger stress amplitude of $q^{\text{ampl}} = 45$ kPa. The GIS parameters used for all the simulations within this paper have been calibrated using these two tests. The

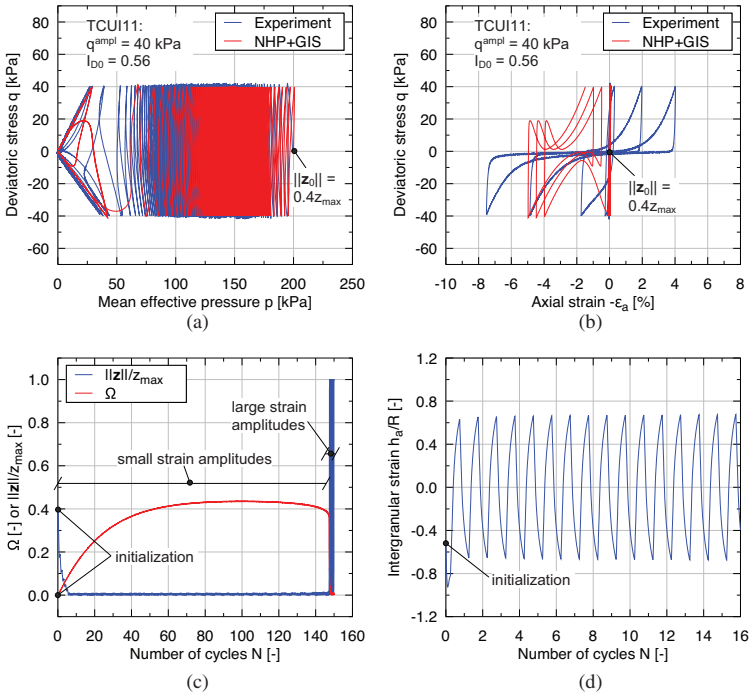

FIGURE 13 | Experimental results [36] versus simulations with NHP+GIS for an undrained cyclic triaxial test on KFS with a prescribed stress amplitude of $q^{\text{ampl}} = 40$ kPa: (a) effective stress path in the pq diagram, (b) deviatoric stress q as a function of the axial strain ε_a, (c) cyclic preloading Ω and norm of the fabric tensor $\|\boldsymbol{z}\|$, and (d) intergranular strain component h_a as a function of the number of cycles N.

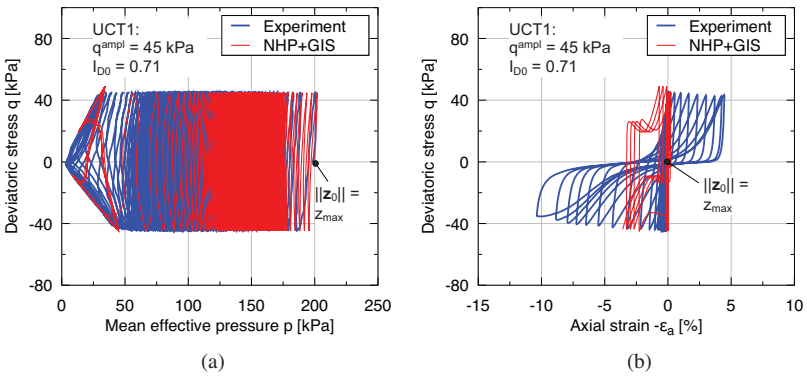

FIGURE 14 | Experimental results [55] versus simulations with NHP+GIS for an undrained cyclic triaxial test on ZS with a prescribed stress amplitude of $q^{\text{ampl}} = 45$ kPa: (a) effective stress path in the pq diagram and (b) deviatoric stress q as a function of the axial strain ε_a.

effective stress paths in the pq diagram in Figures 13a and 14a already indicate good agreement between the simulations and the experiments. After several cycles, the so-called butterfly-shaped stress path is reproduced, although the liquefaction ($p = q = 0$) is not reached perfectly. The stress–strain curves in Figures 13b and 14b are realistic until the butterfly-shaped stress path is reached for the first time. After this moment, the simulations produce an unrealistically pronounced unsymmetrical strain accumulation. Both issues are well-known deficits of hypoplastic constitutive models [25]. They have been recently addressed by [64–66] within the scope of the HP model.

Figure 13c illustrates for the simulation of the KFS the evolution of the CP variable Ω and the norm of the fabric tensor $\|\boldsymbol{z}\|$ as a function of the number of cycles N. During the first few cycles, the fabric decreases, and a build-up of the CP variable occurs. Both effects cause a significant reduction in the accumulation rate. The latter can be seen in detail in Figure 15a, which visualizes the normalized pore fluid pressure p_f / p_0 as a function of the number of cycles N and will be discussed later in detail.

With a decrease in the mean effective pressure, the given stress amplitude leads to an increase in the strain amplitude caused by the reduced stiffness. Consequently, Ω achieves a peak before decreasing again. Once the butterfly-shaped stress path is achieved, $\Omega \approx 0$ is reached rapidly due to large strain amplitudes. The evolution of the norm of the fabric tensor $\|\boldsymbol{z}\|$ shows an inverse trend. At the initial small strain amplitudes, the fabric tensor first degrades to $\|\boldsymbol{z}\| \approx 0$ before it builds up to $\|\boldsymbol{z}\| = z_{\max}$ again (with different sign) between the loading direction reversals in the cyclic mobility phase with large strain amplitudes. The evolution of the IS component h_a within the first cycles is shown

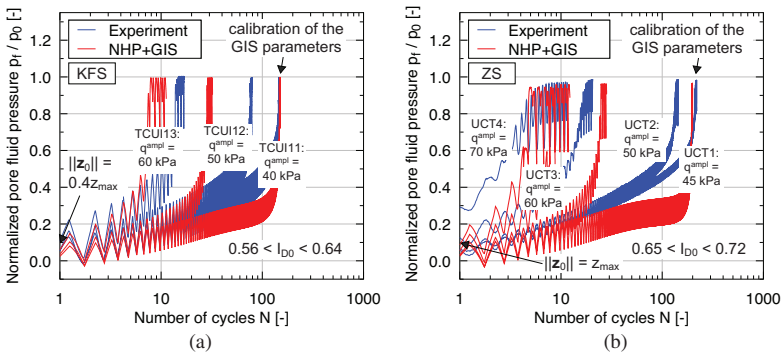

FIGURE 15 | Experimental results [36, 55] versus simulations with NHP+GIS for the normalized pore fluid pressure p_f/p_0 as a function of the number of cycles N in undrained cyclic triaxial tests with different stress amplitudes: (a) KFS and (b) ZS.

in Figure 13d. A pronounced cyclic variation and a fast change after a load direction reversal can be seen. The initialization of the IS is already overwritten after the first cycles with relatively small strain amplitudes and $\rho < 1$.

In addition, further tests with a larger stress amplitudes are considered for each sand. The normalized pore fluid pressure p_f/p_0 as a function of the number of cycles N is shown in Figure 15a for KFS and in Figure 15b for ZS. An increased stress amplitude leads to increased strain amplitudes and to a faster accumulation. The GIS parameters have been calibrated using the tests with the smallest stress amplitude. It can be seen that the number of cycles to reach liquefaction in the additional tests is qualitatively reproduced, although a quantitative difference between the experiments and the simulations can be observed. The fast accumulation at the beginning, the slower accumulation in the middle, and the fast accumulation at the end of the tests, which is not immediately obvious due to the logarithmic scale in Figure 15, should be noted.

6.5 | Undrained Cyclic Triaxial Tests With Prescribed Strain Amplitude

Three undrained cyclic triaxial tests with a prescribed strain amplitude of $\varepsilon_a^{\text{ampl}} = 10^{-2}$ on KFS samples are shown in Figure 16 for three different initial densities. The effective stress paths in the pq diagram are presented in Figure 16a,c,e, while the stress–strain curves are shown in Figure 16b,d,f. It can be observed that cyclic liquefaction ($p = q = 0$) occurs regardless of the initial density, leading to a vanishing shear stiffness and thus $q = 0$ after several cycles. The density of the sample only influences the number of cycles required to reach this state. The denser the soil, the more cycles are necessary. Due to the relatively large strain amplitude, only a few cycles are required to achieve liquefaction and the loosest sample liquefies within the first cycle.

The simulations using the NHP+GIS model qualitatively reproduce this experimentally observed behavior, showing a strong tendency toward cyclic liquefaction. In loose soil, liquefaction is perfectly achieved with $p = q = 0$. In dense soil, however, the model only predicts $p \approx 0$, while still capturing the experimental trends well. The number of cycles up to liquefaction can also be reproduced. Note that the liquefaction of dense soil cannot be modeled by HP+IS.

In contrast, Figure 17 presents an undrained cyclic triaxial test with a prescribed small strain amplitude of $\varepsilon_a^{\text{ampl}} = 6 \cdot 10^{-4}$. Similar to the previous experiments, the soil tends to a cyclic liquefaction state ($p = q = 0$), as observed in the effective stress path in Figure 17a and in the stress–strain response in Figure 17b. While the simulation using NHP+GIS reproduces the stress–strain hysteresis and the onset of liquefaction, it significantly overestimates the accumulation rate. It should be noted that the GIS parameters were not calibrated for this test. Similar deviations in the accumulation rate can be observed in previously discussed results in Figure 15 for tests where the GIS parameters were not specifically calibrated.

6.6 | Stiffness Degradation and Damping

The secant shear stiffness modulus G of soil exhibits a strong dependence on the applied shear strain amplitude γ^{ampl}. At small shear strain amplitudes, the stiffness is considerably higher compared to larger amplitudes. As the shear strain amplitude increases, the material damping ratio D also increases. For small shear strain amplitudes, where the stiffness remains high, damping effects can be considered negligible. This characteristic mechanical behavior of soil plays a crucial role in geotechnical applications [67–69] and should, therefore, be properly accounted for in advanced constitutive models.

To capture these so-called small strain effects, the original IS and the novel GIS concepts are designed. To evaluate the degradation of secant stiffness as a function of the applied shear strain amplitude, as well as the corresponding damping behavior in the novel NHP+GIS model, cyclic simple shear tests are simulated. These tests are characterized by the constraints $\dot{\sigma}_{11} = 0 = \dot{\varepsilon}_{22} = \dot{\varepsilon}_{33} = \dot{\varepsilon}_{13} = \dot{\varepsilon}_{23}$ and a varying shear strain amplitude $\varepsilon_{12}^{\text{ampl}} = 0.5\gamma_{12}^{\text{ampl}}$.

All simulations are based on the parameter set for KFS and assume an isotropic initial stress state of $p_0 = 200$ kPa, a void ratio of $e_0 = 0.75$, an initial IS $\boldsymbol{h}_0 = \mathbf{0}$, an initial fabric of $\boldsymbol{z}_0 = \mathbf{0}$, and an initial CP variable $\Omega_0 = 0$. The secant shear stiffness modulus G and the damping ratio D are derived in the post-processing stage from the resulting hysteretic $\sigma_{12} - \gamma_{12}$ curve using the third cycle of every cyclic simple shear test.

The resulting normalized secant shear modulus $G/G_{\max}$ as a function of the applied shear strain amplitude is shown in

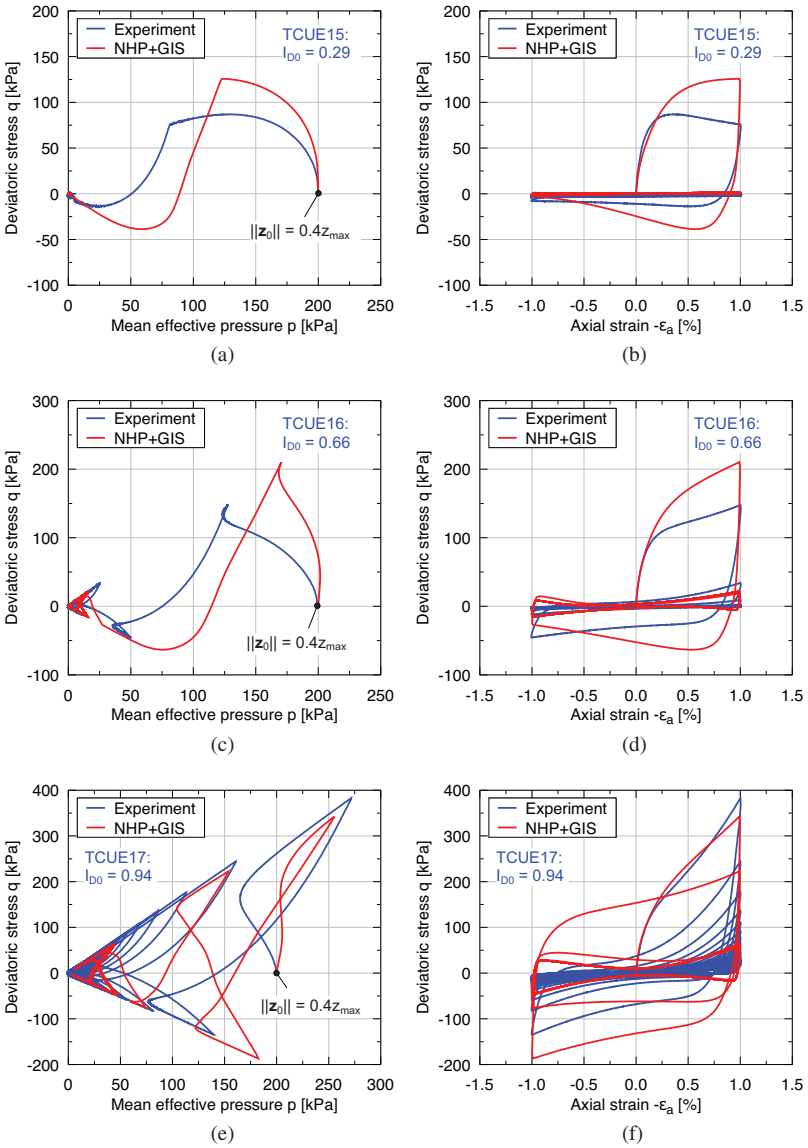

FIGURE 16 | Experimental results [54] versus simulations with NHP+GIS for undrained cyclic triaxial test with a prescribed strain amplitude of $\varepsilon_a^{\text{ampl}} = 10^{-2}$ on KFS samples with varying density: (a, c, and e) effective stress paths in the pq diagram and (b, d, and f) deviatoric stress q as a function of the applied axial strain ε_a.

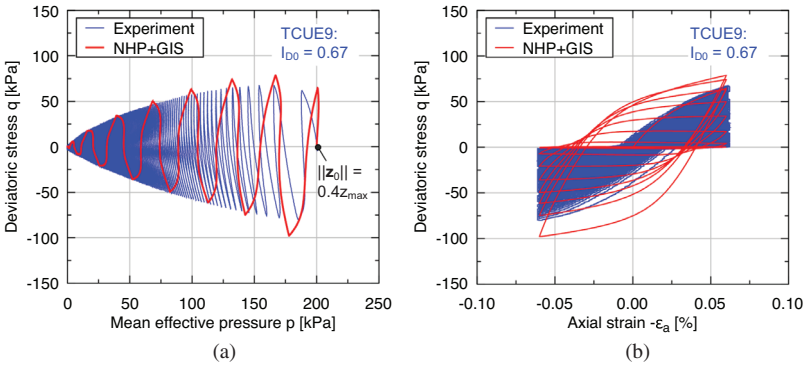

FIGURE 17 | Experimental results [54] versus simulation with NHP+GIS for an undrained cyclic triaxial test with a prescribed strain amplitude of $\varepsilon_a^{\text{ampl}} = 6 \cdot 10^{-4}$ on KFS: (a) effective stress paths in the pq diagram and (b) deviatoric stress q as a function of the applied axial strain ε_a.

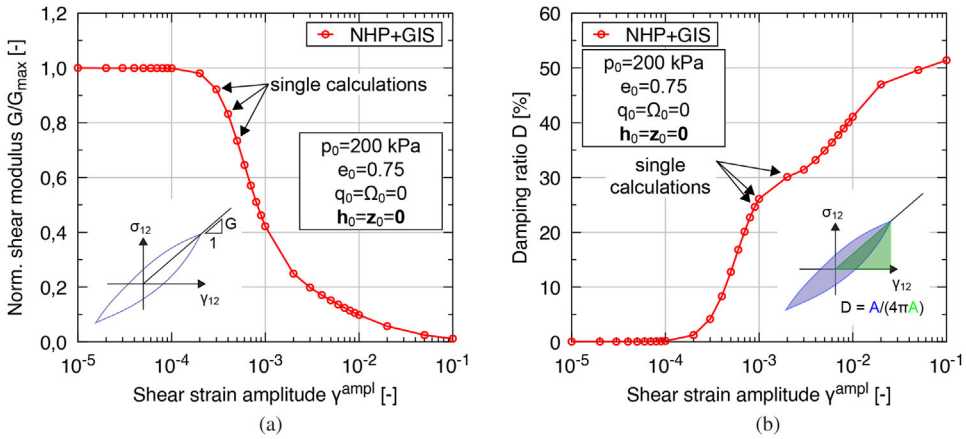

FIGURE 18 | Simulations of cyclic simple shear tests with varying shear strain amplitude γ^{ampl} using the NHP+GIS: (a) normalized secant shear stiffness modulus $G/G_{\max}$ and (b) damping ratio D as a function of the shear strain amplitude $\gamma_{12}^{\text{ampl}}$ for KFS ($p_0 = 200$ kPa, $e_0 = 0.75$, $\boldsymbol{h}_0 = \boldsymbol{z}_0 = \boldsymbol{0}$ and $\Omega_0 = 0$).

Figure 18a, while Figure 18b presents the corresponding damping curve. These figures also provide a graphical representation of the calculation of the secant stiffness modulus G and the damping ratio D. With increasing strain amplitude, the secant shear stiffness decreases, and the corresponding material damping increases. At very small strain amplitudes ($\gamma^{\text{ampl}} < 10^{-4}$), the secant shear stiffness is almost constant and the damping can be neglected in this nearly elastic range. Both curves show the expected trend for soil. One should note, however, that the unrealistic damping curves with local peaks documented for HP+IS, for example, in [26] can also occur in NHP+GIS.

6.7 | Response Envelopes

Constitutive equations of rate type can be represented graphically using so-called response envelopes [70], which are polar diagrams in the stress rate space for unit strain rates. They can be transferred from the stress rate space into the stress space. By doing so, the tangential stiffness predicted by a constitutive model for different strain rate directions can be evaluated graphically for different stress states.

Response envelopes are simulated using NHP+GIS for KFS for axisymmetric stress states for two different void ratios ($e = 0.7$ and $e = 0.9$) and presented in Figure 19 in the pq diagram. For practical purposes, the radius of the strain envelopes used to calculate the stress response is set to $7 \cdot 10^{-5}$. To illustrate the influence of the IS tensor $\boldsymbol{h}$ and the fabric tensor $\boldsymbol{z}$, Figure 19a depicts conditions where $\boldsymbol{z} = \boldsymbol{h} = \boldsymbol{0}$, while Figure 19b considers states with $\boldsymbol{h} = \boldsymbol{0}$ but $\boldsymbol{z} \neq \boldsymbol{0}$, following the fabric initialization for AP samples described earlier. Finally, Figure 19c shows response envelopes where both $\boldsymbol{h}$ and $\boldsymbol{z}$ are initialized according to the AP sample initialization.

The NHP+GIS simulations produce continuous response envelopes. The denser the soil, the higher its stiffness, resulting in larger response envelopes. At isotropic stress states with $\boldsymbol{h} = \boldsymbol{0}$, the material exhibits nearly elastic behavior and the considered state lies close to the center of the response ellipse. For $\boldsymbol{z} \neq \boldsymbol{0}$, the soil behaves anisotropic, which is evident from the shifted points for isochoric shearing in compression and extension direction. When $\boldsymbol{h} \neq \boldsymbol{0}$, the response envelope undergoes a significant shift, clearly demonstrating the stiffness dependency on the direction of the applied strain rate.

For states with higher stress ratios, the response envelope continuously shifts relative to the considered state. At very high stress ratios, the stress state may even lie outside the response envelope, which is generally possible in hypoplastic constitutive models and the case for $Y > 1$.

6.8 | Comparison of NHP and NHP+GIS

It is demonstrated in the previous paragraphs that the coupled NHP+GIS model presented in this paper accurately reproduces the experimentally observed soil behavior under both monotonic and cyclic deformation. However, it should be emphasized that the standalone NHP model itself without a small strain extension model is already able to capture the soil behavior under monotonic deformation quite reliably. To demonstrate this, Figure 20 shows simulations using the standalone NHP model (results from NHP+GIS by setting $m_R = m_T = 1.0$) and experimental results for KFS of the already presented Figures 2a, 5b, 11b, and 15a. In addition to the well-reproduced monotonic curves, the deficits of the standalone NHP model for cyclic loading, which are eliminated by the GIS concept, become evident. The latter manifests in the so-called ratcheting and unrealistic accumulation curves.

7 | Shortcomings of NHP+GIS

In the previous section, numerous element test simulations of the novel NHP+GIS constitutive model and their comparison with experimental data have been presented. In general, the constitutive model reproduces the experimental data quite well and at least qualitatively reflects the soil behavior holistically. However, the novel NHP+GIS still exhibits several issues, which have to be known and understood by a practical user and which will be part of future research:

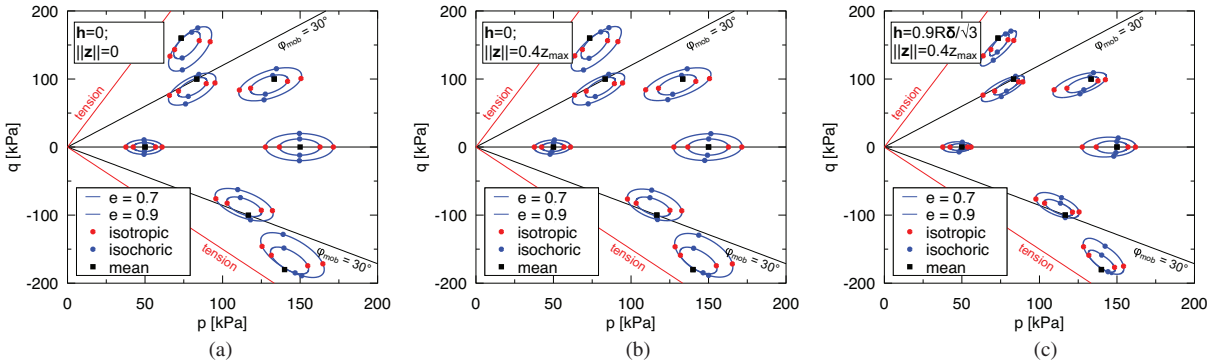

FIGURE 19 | Response envelopes for the coupled NHP+GIS model for different stress states and void ratios under axisymmetric conditions in the pq diagram for (a) $\boldsymbol{h} = \boldsymbol{z} = \boldsymbol{0}$, (b) $\boldsymbol{h} = \boldsymbol{0}$ with $z_a = -0.04 z_{\max} = -2 z_r$, and (c) $\boldsymbol{h} = -0.9 R\boldsymbol{\delta}/\sqrt{3}$ with $z_a = -0.04 z_{\max} = -2 z_r$ ($\Omega = 0$).

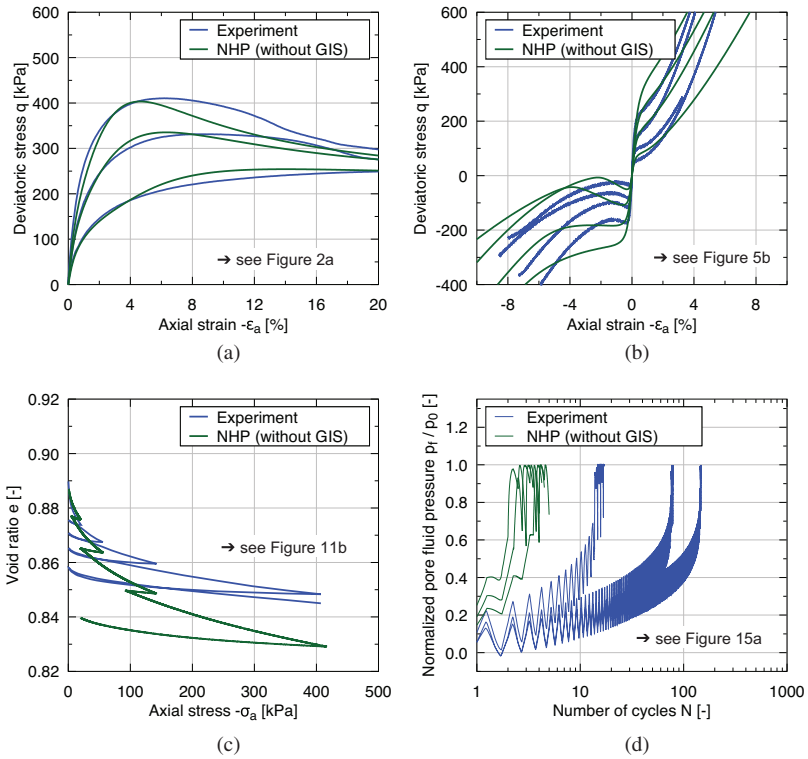

FIGURE 20 | Experimental results [36, 54] versus simulations with NHP (without GIS) for test already considered including monotonic and cyclic deformations on KFS.

- Undershooting/ratcheting: Although the GIS concept addresses ratcheting in general, it can only prevent the latter for a certain amplitude range for which the parameters have been calibrated. In cyclic deformations with deviating amplitudes, ratcheting/undershooting can still occur. This issue can lead in practical simulations to an overestimation of the accumulation effects, as can be seen for example in Figure 17. It should also be mentioned that the effect of the GIS extension is very small at high stress ratios where $Y \approx 1$ applies. In such conditions, ratcheting may occur. Compared to other base models, the stress range with $Y \approx 1$ is rather large in NHP.
- Overshooting of nonlimit states: The GIS concept is coupled with the NHP using the degree on nonlinearity Y. Doing so, the overshooting of the limit state due to a small un- and reloading is prevented. However, overshooting of other asymptotic states is not prevented. The latter could be done by including the ASBS using the state mobilization S in the govern equations [5], which is for the NHP currently not possible due to the lack of the extracted ASBS.
- Unrealistic cyclic mobility: The simulations of the cyclic mobility phase in an undrained cyclic triaxial test with a given stress amplitude show some flaws, as it can be seen in Figures 13 and 14. On the one hand, the "wings" of the butterfly in the effective stress path are too large, and on the other hand, the stress–strain curve show an unrealistic shape. Furthermore, a constant strain amplitude and a

one-sided accumulation in the extension direction occur, which also contradicts the experimental data.

- Unrealistic damping curves: For an unfavorable combination of the state of the soil and the chosen constitutive parameters, damping curves (damping ratio D as a function of the applied shear strain amplitude γ^{ampl}) with unrealistic shapes, for example, local peak values, can be obtained. This deficit has already been documented in [26] for the original IS concept.
- Violation of the consistency condition of isotropic compression [71]: NHP and thus also NHP+GIS does not tend to the void ratio $e_i(P)$ described by Equation (4) due to monotonic proportional isotropic compression. In contrast, all critical states calculated by the model lie on the curve $e_c(P)$ according to Equation (4). Numerical simulations have shown that for large and practically not relevant pressures, the isotropic compression line predicted by NHP can fall below the critical state line $e_c(P)$ in the ep diagram, which does not correspond to the experimental observation.

8 | Shear Band Bifurcation

After the coupled model NHP+GIS has been calibrated using the comparison of element test simulations with experimental test data, the solution of a boundary value problem (BVP) is discussed to demonstrate the practical applicability of the novel constitutive model. The following quasi-static finite element analyses on dry sand have been solved using the commercial program *Abaqus*. The NHP+GIS could be considered using the same *umat.for* implementation used for the already presented element test simulations.

The sudden formation of a shear band, which is also known as bifurcation problem, is considered. Thereby, a localization of strains occurs within the shear band. The theoretical problem of bifurcation in hypoplastic models is discussed in detail in the literature [72–75] and corresponding numerical simulations can be found in [76, 77]. It is worth mentioning that the onset of strain localization is not deterministic. The latter may or may not occur and is one optional solution of a corresponding BVP [4]. For incrementally nonlinear constitutive models, a necessary condition for the onset of shear banding can be derived. Shear banding may occur beyond but not inside of the so-called bifurcation surface [4, 74, 75].

In the present paper, the shear band bifurcation is shown in 2D plane strain conditions (biaxial compression) using the NHP+GIS constitutive formulation for one specific mesh density only, which controls shear band characteristics (a study of the discretization effect is out of scope of this paragraph). ZS parameters are used. The corresponding BVP is visualized in Figure 21. The latter is theoretically motivated and the results will not be compared with experimental data. A soil body with an aspect ratio of $h/b = 2$ is considered, which is loaded on the vertical boundaries with a constant pressure of $t_1 = 100$ kPa in the horizontal direction (x_1). The boundary at the bottom is fixed in the vertical direction ($u_2 = 0$). A monotonic vertical displacement of $u_2(t)$ is defined at the boundary at the top of the model. Starting from $u_2 = 0$, $u_2 = h/10$ is reached at the end of the simulation. Shear stresses are prohibited at any boundary. To

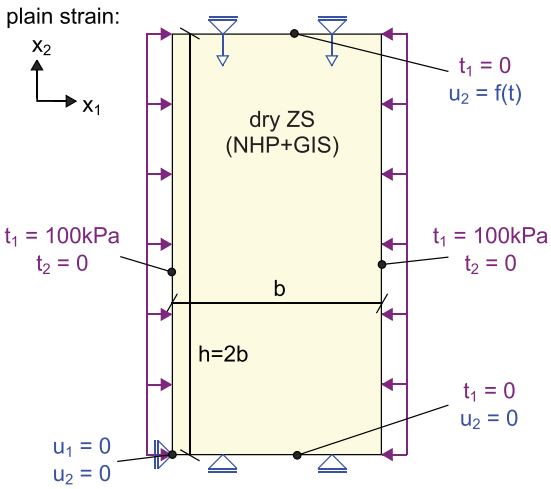

FIGURE 21 | BVP of the analyzed shear band bifurcation under 2D plane strain conditions (biaxial compression) using NHP+GIS.

avoid a kinematic mechanism, the node in the left bottom corner is fixed in the horizontal direction ($u_1 = 0$).

The presented simulation is based on an isotropic and uniform initial stress state of $p_0 = 100$ kPa, an initial void ratio of $e_0 = 0.55$ (dense sand), an initial IS of $\boldsymbol{h}_0 = \mathbf{0}$ and an initial CP variable of $\Omega_0 = 0$. Three different values of the initial fabric are considered. $\boldsymbol{z}_0 = \mathbf{0}$ is chosen as the reference variant. Two further simulations with an initialized fabric of $z_1 = -z_2 = z_{max}/\sqrt{2}$ (sedimentation in x_2 direction) and $-z_1 = z_2 = z_{max}/\sqrt{2}$ (sedimentation in x_1 direction) are performed. Gravity is neglected. 1732 CPE4 elements are used. Note that no weak element was defined, so the onset of bifurcation is an implicit result of the simulations. Whether the calculation in *Abaqus* continues or aborts after the bifurcation depends, decisively, on the chosen Jacobian, which was estimated in the simulations shown using $\overline{\mathrm{E}}\, m_R$.

It is worth mentioning the dependency of the results on the spatial discretization in the numerical simulations of the shear band formation. The results are fully mesh-dependent since the NHP+GIS do not include a characteristic length [78, 79]. Nevertheless, this simple problem highlights the applicability of NHP+GIS to complex BVPs. Before bifurcation, the solution corresponds to an element test simulation with homogeneous fields. However, after bifurcation, the solution exhibits inhomogeneous fields of all state variables.

The spatial distribution of the void ratio e, the norm of the fabric tensor $\|\boldsymbol{z}\|$, and the degree of nonlinearity Y at the end of the simulation of the reference variant is shown in Figure 22. Note that the latter does not represent a state variable of the NHP+GIS, however, it indicates the intensity of irreversible deformation. It is evident that the fields depicted in Figure 22 are not spatially distributed homogeneously, that is,

$$\frac{\partial \boldsymbol{\alpha}}{\partial \boldsymbol{x}} \neq 0 \tag{32}$$

applies for any state variable $\boldsymbol{\alpha}$ at least in an area of the soil (shear band). The strain localization is obvious in Figure 22a. The void ratio inside the shear band is substantially larger compared

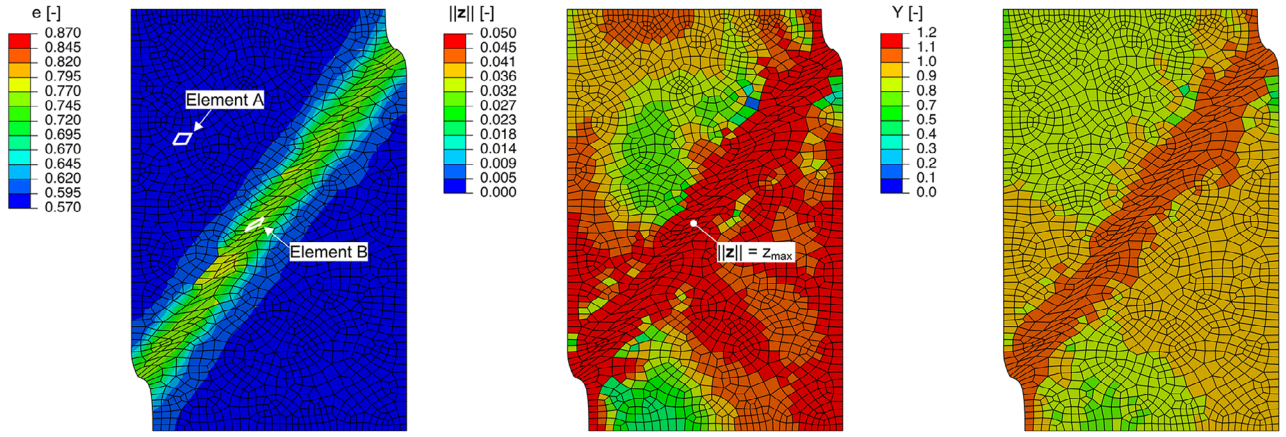

FIGURE 22 | Spatial distribution of (a) the void ratio e, (b) the norm of the fabric tensor $\|\boldsymbol{z}\|$, and (c) the degree of nonlinearity Y at the end of the simulated biaxial compression ($p_0 = 100$ kPa, $e_0 = 0.55$, $\boldsymbol{h}_0 = \boldsymbol{z}_0 = \mathbf{0}$, $\Omega_0 = 0$).

to outside. In other words, beginning with homogeneous fields, nonhomogeneous fields of the state variables occurred during the calculation. Thus, a bifurcation appeared.

As discussed in [24], the fabric tensor $\boldsymbol{z}$ can be interpreted as the rolling of individual grains. Figure 22b illustrates that inside the shear band, a maximum value of the fabric tensor is reached, whereas outside, the latter is smaller. A micro-mechanical rolling of individual grains leading to a pronounced anisotropic fabric inside of the shear band can be described qualitatively using NHP+GIS. These micro-mechanical observations derived from NHP+GIS correspond to current experimental work, which uses x-ray tomography to allow micro-mechanical observations during soil shearing. A rolling of grains inside the shear band was recently documented, for example, by [63].

The concentration of the irreversible deformations in the shear band can also be detected by the higher degree of nonlinearity, as shown in Figure 22b.

The bifurcation phenomenon is investigated in more detail in Figure 23 using the evolution of selected state variables as a function of the applied relative deformation. Two selected finite elements are considered further: Element A is located outside and Element B is located inside of the shear band. Both are highlighted in Figure 22a. A perfect numerical element test, meaning just the integration of the constitutive model for a drained biaxial compression using *IncrementalDriver*, is simulated for comparison.

The stress components σ_{11} and σ_{22} in the global coordinate system are shown for each of the four integration points (IPs) for the two elements and the element test in the Figures 23a and 23b. It can be seen that at the beginning of the simulation, the evolution of the stress components is identical in all IPs and also in the element test. In this calculation phase, no bifurcation has yet taken place and the spatial distribution of the state variables is still homogeneous. After a certain amount of deformation, there is a sudden deviation of the stress components between the elements and even between the IPs. At this point, the bifurcation occurs, that is, the strain localization takes place. As a result, the spatial fields of the state variables lose their initial homogeneity.

Of particular interest is the evolution of the void ratio, which is shown in Figure 23c. After bifurcation, the latter rapidly converges to the critical void ratio $e_c(P)$ inside the shear band. Measured in global deformation, this happens significantly faster than in the element test simulation. Outside of the shear band, the void ratio remains approximately constant after the bifurcation.

Finally, Figure 23d shows the evolution of the norm of the fabric tensor $\|\boldsymbol{z}\|$. The maximum value $z_{\max}$ results within the shear band, while outside of the shear band, the corresponding value is smaller and tends to decrease. As already discussed in 22b, this can be qualitatively attributed to the micro-mechanical rolling of grains, which is expected to be much more pronounced inside of the shear band than outside.

It is also visible that changes in the state variables occur after the bifurcation, both within and outside the shear band, which is solely a consequence of a nonvanishing strain rate $\dot{\boldsymbol{\varepsilon}}$ outside the shear band as well.

The evolution of the stress component σ_{22} and the void ratio e for the variants with different initializations of the fabric tensor are shown in Figure 24. It becomes obvious that the onset of shear band formation takes place at a different values of the applied deformation (strain). The greater the deviation between the direction of loading (x_2 direction) and the direction of sedimentation, the greater the contraction of the sample at the beginning of the simulation and the larger the required deformation until the onset of the bifurcation. However, the overall state of the soil at the onset of shear band formation is practically identical in all calculations.

9 | Conclusion

This paper presents the coupling of the advanced hypoplastic sand model called NHP with the concept of the GIS to describe the mechanical behavior of sand under monotonic and cyclic

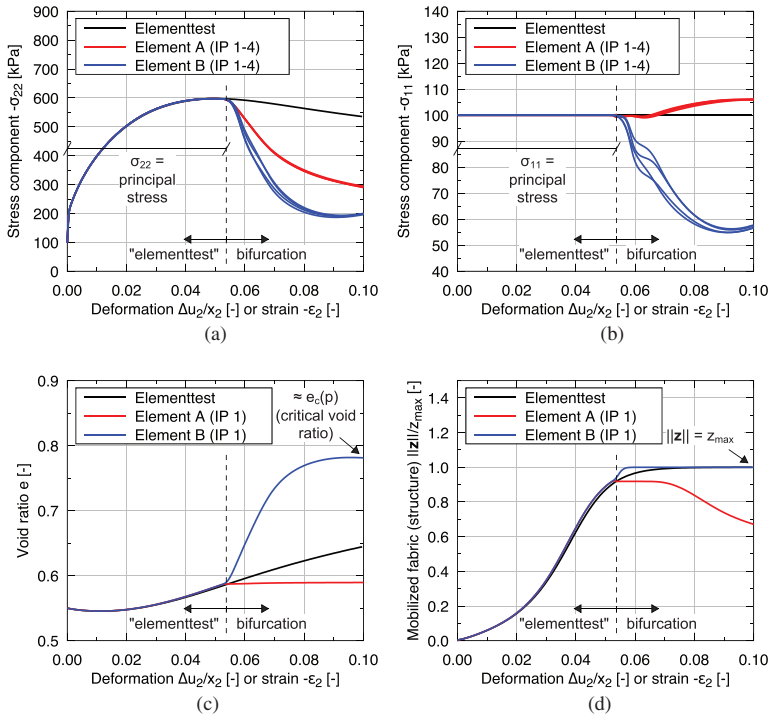

FIGURE 23 | Evolution of selected state variables in Element A outside and Element B inside the shear band and comparison with a real element test simulation: (a) stress component σ_{11}, (b) stress component σ_{22}, (c) void ratio e, and (d) norm of the fabric tensor $\|\boldsymbol{z}\|$ as a function of the corresponding deformation ($p_0 = 100$ kPa, $e_0 = 0.55$, $\boldsymbol{h}_0 = \boldsymbol{z}_0 = \boldsymbol{0}$, $\Omega_0 = 0$).

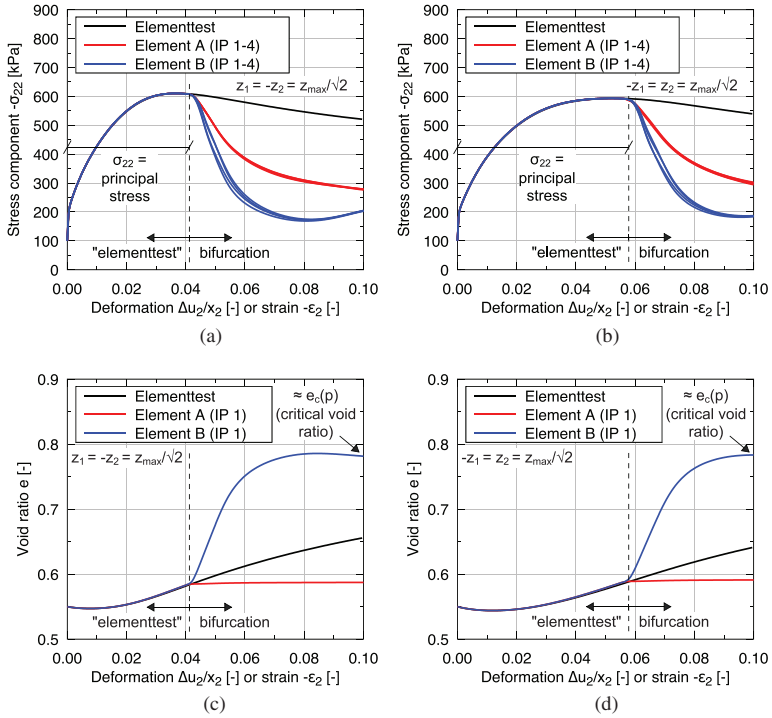

FIGURE 24 | Evolution of state variables in Element A outside and Element B inside the shear band and comparison with a real element test simulation: (a, b) stress component σ_{22}, and (c, d) void ratio e as a function of the corresponding deformation for different initializations of the fabric tensor ($z_1 = -z_2 = z_{max}/\sqrt{2}$ (sedimentation in x_2 direction) and $-z_1 = z_2 = z_{max}/\sqrt{2}$ (sedimentation in x_1 direction)).

loading. The coupled NHP+GIS model effectively describes soil behavior, incorporating the following five state variables: (a) effective Cauchy-stress $\boldsymbol{\sigma}$, (b) void ratio e, (c) fabric/structure tensor $\boldsymbol{z}$, (d) IS $\boldsymbol{h}$, and (e) CP variable Ω.

Guidance on the calibration of the 11 NHP and the 10 GIS parameters is provided, with calibration performed using experimental data on KFS and ZS. Element test simulations demonstrate the model's ability to reproduce the experimentally observed mechanical behavior across various void ratios and mean effective pressures for both monotonic and cyclic tests. While the model accurately captures monotonic drained behavior and accumulation effects, some limitations in reproducing the monotonic undrained stress path and the butterfly effect due to cyclic loading remain.

A finite element analysis of the shear band bifurcation due to biaxial compression is conducted and demonstrate the application of the NHP+GIS in an initial BVP. It is shown that the NHP+GIS reproduces the experimentally observed rolling of grains within the shear band.

Author Contributions

Luis Mugele: conceptualization, methodology, software, formal analysis, investigation, writing – original draft, visualization, funding acquisition. **Hans Henning Stutz**: conceptualization, methodology, resources, writing – review and editing, supervision, project administration, funding acquisition. **David Mašín**: conceptualization, methodology, validation, resources, writing – review and editing, supervision, project administration, funding acquisition.

Acknowledgments

The first author acknowledges the research travel grant from Karlsruhe House of Young Scientists (KHYS) for the financial support for the stay at Charles University Prague. The first author would also like to express gratitude to the entire team at Charles University Prague for their gracious hospitality. The third author is grateful for the financial support provided by the grant INTER-COST No. LUC24143 of the Czech Ministry of Education, Youth and Sports. We appreciate the detailed comments of the two reviewers, which considerably improved our work.

Open access funding enabled and organized by Projekt DEAL.

Conflicts of Interest

The authors declare no conflicts of interest.

Data Availability Statement

The data that support the findings of this study are available from the corresponding author upon reasonable request.

Endnotes

[1] In the special cases of (a) $\boldsymbol{f}(\dot{\boldsymbol{\varepsilon}}, \boldsymbol{\alpha}) = \mathbf{0}$ and $C = 0$, $S = 0$, or $\boldsymbol{m} = \mathbf{0}$ and (b) $\boldsymbol{f}(\dot{\boldsymbol{\varepsilon}}, \boldsymbol{\alpha}) = \boldsymbol{m}\, C\, S\, \|\dot{\boldsymbol{\varepsilon}}\|$, Equation (1) becomes incrementally linear.

[2] Precisely, under axisymmetric conditions, $z_{a0} = 0.016 = 2z_{r0}$ ($\|\boldsymbol{z}_0\| = 0.392 z_{\max}$) and $z_{a0} = 0.04 = 2z_{r0}$ ($\|\boldsymbol{z}_0\| = 0.98 z_{\max}$) is initialized.

References

1. D. Kolymbas and G. Medicus, "Genealogy of Hypoplasticity and Barodesy," *International Journal for Numerical and Analytical Methods in Geomechanics* 40, no. 18 (2016): 2532–2550, https://doi.org/10.1002/nag.2546.

2. D. Mašín, *Modelling of Soil Behaviour With Hypoplasticity* (Springer International Publishing, 2019).

3. W. Wu and D. Kolymbas, "Hypoplasticity Then and Now," in *Constitutive Modelling of Granular Materials*, ed. D. Kolymbas (Springer, 2000), 57–105.

4. A. Niemunis, "*Extended Hypoplastic Models for Soils*," (Habil., Ruhr-Universität Bochum, Institut für Grundbau und Bodenmechanik, 2003). issue no. 34.

5. L. Mugele, H. H. Stutz, and D. Mašín, "Generalized Intergranular Strain Concept and Its Application to Hypoplastic Models," *Computers and Geotechnics* 173 (2024): 106480, https://doi.org/10.1016/j.compgeo.2024.106480.

6. A. Niemunis, C. E. Grandas-Tavera, and L. F. Prada-Sarmiento, "Anisotropic Visco-Hypoplasticity," *Acta Geotechnica* 4, no. 4 (2009): 293–314, https://doi.org/10.1007/s11440-009-0106-3.

7. M. Tafili and T. Triantafyllidis, "AVISA: Anisotropic Visco-ISA Model and Its Performance at Cyclic Loading," *Acta Geotechnica* 15, no. 9 (2020): 2395–2413, https://doi.org/10.1007/s11440-020-00925-9.

8. C. Tamagnini and G. Viggiani, "Constitutive Modelling for Rate-Independent Soils: A Review," *Revue Française de Génie Civil* 6, no. 6 (2002): 933–974, https://doi.org/10.1080/12795119.2002.9692726.

9. P.-A. von Wolffersdorff, "A Hypoplastic Relation for Granular Materials With a Predefined Limit State Surface," *Mechanics of Cohesive-frictional Materials* 1, no. 3 (1996): 251–271, https://doi.org/10.1002/(SICI)1099-1484(199607)1:3⟨251::AID-CFM13⟩3.0.CO;2-3.

10. E. Bauer, "Calibration of a Comprehensive Hypoplastic Model for Granular Materials," *Soils and Foundations* 36, no. 1 (1996): 13–26, https://doi.org/10.3208/sandf.36.13.

11. C, E. Grandas-Tavera, T. Triantafyllidis, and L. Knittel, "A Constitutive Model With a Historiotropic Yield Surface for Sands," in *Recent Developments of Soil Mechanics and Geotechnics in Theory and Practice*, ed. T. Triantafyllidis (Springer, 2020), 13–43.

12. G. Gudehus, "A Comprehensive Constitutive Equation for Granular Materials," *Soils and Foundations* 36, no. 1 (1996): 1–12, https://doi.org/10.3208/sandf.36.1.

13. D. Kolymbas, "A Rate-Dependent Constitutive Equation for Soils," *Mechanics Research Communications* 4, no. 6 (1977): 367–372, https://doi.org/10.1016/0093-6413(77)90056-8.

14. W. Wu and E. Bauer, "A Simple Hypoplastic Constitutive Model for Sand," *International Journal for Numerical and Analytical Methods in Geomechanics* 18, no. 12 (1994): 833–862, https://doi.org/10.1002/nag.1610181203.

15. D. Mašín, "A Hypoplastic Constitutive Model for Clays," *International Journal for Numerical and Analytical Methods in Geomechanics* 29, no. 4 (2005): 311–336, https://doi.org/10.1002/nag.416.

16. D. Mašín, "Hypoplastic Cam-Clay Model," *Géotechnique* 62, no. 6 (2012): 549–553, https://doi.org/10.1680/geot.11.T.019.

17. D. Mašín, "Clay Hypoplasticity With Explicitly Defined Asymptotic States," *Acta Geotechnica* 8, no. 5 (2013): 481–496, https://doi.org/10.1007/s11440-012-0199-y.

18. D. Mašín, "Clay Hypoplasticity Model Including Stiffness Anisotropy," *Géotechnique* 64, no. 3 (2014): 232–238, https://doi.org/10.1680/geot.13.P.065.

19. A. Niemunis and I. Herle, "Hypoplastic Model for Cohesionless Soils With Elastic Strain Range," *Mechanics of Cohesive-frictional Materials* 2, no. 4 (1997): 279–299, https://doi.org/10.1002/(SICI)1099-1484(199710)2:4⟨279::AID-CFM29⟩3.0.CO;2-8.

20. S. Chrisopoulos and J. Vogelsang, "A Finite Element Benchmark Study Based on Experimental Modeling of Vibratory Pile Driving in

Saturated Sand," *Soil Dynamics and Earthquake Engineering* 122 (2019): 248–260, https://doi.org/10.1016/j.soildyn.2019.01.001.

21. P. Norlyk, K. Sørensen, L. V. Andersen, K. K. Sørensen, and H. H. Stutz, "Holistic Simulation of a Subsurface Inflatable Geotechnical Energy Storage System Using Fluid Cavity Elements," *Computers and Geotechnics* 127 (2020): 103722, https://doi.org/10.1016/j.compgeo.2020.103722.

22. P. Staubach, J. Machaček, and T. Wichtmann, "Large-Deformation Analysis of Pile Installation With Subsequent Lateral Loading: and vs. Sanisand, Hypoplasticity," *Soil Dynamics and Earthquake Engineering* 151 (2021): 106964, https://doi.org/10.1016/j.soildyn.2021.106964.

23. M. Tafili, J. Duque, D. Mašín, and T. Wichtmann, "Repercussion of Overshooting Effects on Elemental and Finite-Element Simulations," *International Journal of Geomechanics* 24, no. 3 (2024): 06024001, https://doi.org/10.1061/IJGNAI.GMENG-8842.

24. L. Mugele, A. Niemunis, and H. H. Stutz, "Neohypoplasticity Revisited," *International Journal for Numerical and Analytical Methods in Geomechanics* 48, no. 1 (2024): 311–331, https://doi.org/10.1002/nag.3640.

25. J. Duque, M. Yang, W. Fuentes, D. Mašín, and M. Taiebat, "Characteristic Limitations of Advanced Plasticity and Hypoplasticity Models for Cyclic Loading of Sands," *Acta Geotechnica* 17, no. 6 (2022): 2235–2257, https://doi.org/10.1007/s11440-021-01418-z.

26. L. F. Prada-Sarmiento, "Paraelastic Description of Small-Strain Soil Behaviour" (Diss., Karlsruher Institut für Technologie, Institut für Bodenmechanik und Felsmechanik, 2011). issue no. 173.

27. A. Niemunis and C. E. Grandas-Tavera, "Essential Concepts of Neohypoplasticity," in *Desiderata Geotechnica*, ed. W. Wu (Springer eBooks Engineering, 2019), 132–142.

28. A. Niemunis, C. E Grandas Taverna, and T. Wichtmann, "Peak Stress Obliquity in Drained and Undrained Sands. Simulations With Neohypoplasticity," in *Holistic Simulation of Geotechnical Installation Processes: Benchmarks and Simulations*, ed. T. Triantafyllidis (Springer International Publishing, 2016), 85–114.

29. J. Duque, D. Mašín, and W. Fuentes, "Improvement to the Intergranular Strain Model for Larger Numbers of Repetitive Cycles," *Acta Geotechnica* 15, no. 12 (2020): 3593–3604, https://doi.org/10.1007/s11440-020-01073-w.

30. W. Fuentes and T. Triantafyllidis, "ISA Model: A Constitutive Model for Soils With Yield Surface in the Intergranular Strain Space," *International Journal for Numerical and Analytical Methods in Geomechanics* 39, no. 11 (2015): 1235–1254, https://doi.org/10.1002/nag.2370.

31. M. Poblete, W. Fuentes, and T. Triantafyllidis, "On the Simulation of Multidimensional Cyclic Loading With Intergranular Strain," *Acta Geotechnica* 11, no. 6 (2016): 1263–1285, https://doi.org/10.1007/s11440-016-0492-2.

32. D. Wegener and I. Herle, "Prediction of Permanent Soil Deformations Due to Cyclic Shearing With a Hypoplastic Constitutive Model," *geotechnik.* 37, no. 2 (2014): 113–122, https://doi.org/10.1002/gete.201300013.

33. N. Irani, L. F. Prada-Sarmiento, M. Tafili, M. Salimi, T. Wichtmann, and T. Triantafyllidis, "Assessment of Free Energy Functions for Sand," *International Journal for Numerical and Analytical Methods in Geomechanics* 49, no. 1 (2025): 132–150, https://doi.org/10.1002/nag.3852.

34. H. Matsuoka and T. Nakai, "Stress-Strain Relationship of Soil Based on the SMP, Constitutive Equations of Soils," in *Speciality Session 9*, ed. S. Murayama and A. N. Schofield (1977).

35. T. Wichtmann, "Soil Behaviour Under Cyclic Loading - Experimental Observations, Constitutive Description and Applications," (Habil., Karlsruher Institut für Technologie, Institut für Bodenmechanik und Felsmechnik, 2016). issue no. 181.

36. T. Wichtmann and T. Triantafyllidis, "An Experimental Database for the Development, Calibration and Verification of Constitutive Models for Sand With Focus to Cyclic Loading: Part I—Tests With Monotonic Loading and Stress Cycles," *Acta Geotechnica* 11, no. 4 (2016): 739–761, https://doi.org/10.1007/s11440-015-0402-z.

37. S. Miura and S. Toki, "Anisotropy in Mechanical Properties and Its Simulation of Sands Sampled From Natural Deposits," *Soils and Foundations* 24, no. 3 (1984): 69–84.

38. M. Oda, "Initial Fabrics and Their Relations to Mechanical Properties of Granular Material," *Soils and Foundations* 12, no. 1 (1972): 17–36.

39. Z. X. Yang, X. S. Li, and J. Yang, "Quantifying and Modelling Fabric Anisotropy of Granular Soils," *Géotechnique* 58, no. 4 (2008): 237–248, https://doi.org/10.1680/geot.2008.58.4.237.

40. J. Arthur and B. K. Menzies, "Inherent Anisotropy in Sand," *Géotechnique* 22, no. 1 (1972): 115–128, https://doi.org/10.1680/geot.1972.22.1.115.

41. H. Ochiai and P. V. Lade, "Three-Dimensional Behavior of Sand With Anisotropic Fabric," *Journal of Geotechnical Engineering, ASCE* 109, no. 10 (1983): 1313–1328.

42. M. Yoshimine, K. Ishihara, and W. Vargas, "Effects of Principal Stress Direction and Intermediate Principal Stress on Undrained Shear Behavior of Sand," *Soils and Foundations* 38, no. 3 (1998): 179–188, https://doi.org/10.3208/sandf.38.3_179.

43. A. Niemunis and C. E. Grandas-Tavera, "Computer Aided Calibration, Benchmarking and Check-Up of Constitutive Models for Soils. Some Conclusions for Neohypoplasticity," in *Holistic Simulation of Geotechnical Installation Processes. Theoretical Results and Applications*, ed. T. Triantafyllidis (Springer, 2017), 168–192.

44. J. Zürn, L. Mugele, and H. H. Stutz, "Novel Experimental Method for Rate-Independent Triaxial Tests Under Partial Drainage Condition," *Géotechnique Letters* 14, no. 3 (2024): 100–105, https://doi.org/10.1680/jgele.23.00120.

45. Y. F. Dafalias and M. T. Manzari, "Simple Plasticity Sand Model Accounting for Fabric Change Effects," *Journal of Engineering Mechanics* 130, no. 6 (2004): 622–634, https://doi.org/10.1061/(ASCE)0733-9399(2004)130:6(622).

46. T. Hueckel and R. Nova, "Some Hysteresis Effects of the Behaviour of Geologic Media," *International Journal of Solids and Structures* 15, no. 8 (1979): 625–642, https://doi.org/10.1016/0020-7683(79)90076-3.

47. R. Nova and T. Hueckel, "An Engineering Theory of Soil Behaviour in Unloading and Reloading," *Meccanica* 16, no. 3 (1981): 136–148, https://doi.org/10.1007/BF02128442.

48. A. Niemunis, L. F. Prada-Sarmiento, and C. E. Grandas-Tavera, "Paraelasticity," *Acta Geotechnica* 6, no. 2 (2011): 67–80, https://doi.org/10.1007/s11440-011-0137-4.

49. J. Duque, M. Tafili, and D. Mašín, "On the Influence of Cyclic Preloadings on the Liquefaction Resistance of Sands: A Numerical Study," *Soil Dynamics and Earthquake Engineering* 172 (2023): 108025, https://doi.org/10.1016/j.soildyn.2023.108025.

50. A. Niemunis, T. Wichtmann, and T. Triantafyllidis, "A High-Cycle Accumulation Model for Sand," *Computers and Geotechnics* 32, no. 4 (2005): 245–263, https://doi.org/10.1016/j.compgeo.2005.03.002.

51. I. Herle, "Hypoplastizität und Granulometrie einfacher Korngerüste" (Diss., Universität Fridericiana in Karlsruhe, Institut für Bodenmechanik und Felsmechnik, 1997). issue no. 142.

52. I. Herle and G. Gudehus, "Determination of Parameters of a Hypoplastic Constitutive Model From Properties of Grain Assemblies," *Mechanics of Cohesive-frictional Materials* 4, no. 5 (1999): 461–486, https://doi.org/10.1002/(SICI)1099-1484(199909)4:5⟨461::AID-CFM71⟩3.0.CO;2-P.

53. T. Wichtmann and T. Triantafyllidis, "An Experimental Database for the Development, Calibration and Verification of Constitutive Models for Sand With Focus to Cyclic Loading: Part II—Tests With Strain Cycles and Combined Loading," *Acta Geotechnica* 11, no. 4 (2016): 763–774, https://doi.org/10.1007/s11440-015-0412-x.

54. J. Opršal, "Cyclic Soil Behavior – Numerical Modelling and Laboratory Testing" (Diploma thesis, Charles University, 2022). unpublished.

55. J. Duque, J. Roháč, and D. Mašín, "On the Influence of Drained Cyclic Preloadings on the Cyclic Behaviour of Zbraslav Sand," *Soil Dynamics and Earthquake Engineering* 165 (2023): 107666, https://doi.org/10.1016/j.soildyn.2022.107666.

56. J. Duque, J. Roháč, D. Mašín, J. Najser, and J. Opršal, "The Influence of Cyclic Preloadings on Cyclic Response of Zbraslav Sand," *Soil Dynamics and Earthquake Engineering* 166 (2023): 107720, https://doi.org/10.1016/j.soildyn.2022.107720.

57. Soilmodels, 2025, www.soilmodels.com.

58. T. Wichtmann, 2025, www.torsten-wichtmann.de.

59. A. Niemunis, IncrementalDriver: programmer's manual (2022), https://soilmodels.com/download/incrementaldriver-zip/.

60. S. Miura and S. Toki, "A Sample Preparation Method and Its Effect on Static and Cyclic Deformation-Strength Properties of Sand," *Soils and Foundations* 22, no. 1 (1982): 61–77, https://doi.org/10.3208/sandf1972.22.61.

61. L. Mugele, Zürn J, A. Niemunis, and H. H. Stutz, "Experimental Study of the Soil Structure Variable z Used in Constitutive Models Such as Neohypoplasticity or Sanisand," *IOP Conference Series: Earth and Environmental Science* 1480 (2025): 012070.

62. T. Wichtmann, K. Steller, and T. Triantafyllidis, "On the Influence of the Sample Preparation Method on Strain Accumulation in Sand Under High-Cyclic Loading," *Soil Dynamics and Earthquake Engineering* 131 (2020): 106028, https://doi.org/10.1016/j.soildyn.2019.106028.

63. S. Schmidt, M. Wiebicke, and I. Herle, "On the Determination and Evolution of Fabric in Representative Elementary Volumes for a Sand Specimen in Triaxial Compression," *Granular Matter* 24, no. 4 (2022): 1–9, https://doi.org/10.1007/s10035-022-01262-2.

64. D. Liao and Z. X. Yang, "Hypoplastic Model for Sand Under Multi-directional Shearing Conditions Considering Fabric Change Effect," *Soil Dynamics and Earthquake Engineering* 155 (2022): 107168, https://doi.org/10.1016/j.soildyn.2022.107168.

65. D. Liao, Z. Yang, S. Wang, and W. Wu, "Hypoplastic Model With Fabric Change Effect and Semifluidized State for Post–Liquefaction Cyclic Behavior of Sand," *International Journal for Numerical and Analytical Methods in Geomechanics* 46, no. 17 (2022): 3154–3177, https://doi.org/10.1002/nag.3444.

66. M. Tafili, J. Duque, D. Mašín, and T. Wichtmann, "A Hypoplastic Model for Pre- and Post-Liquefaction Analysis of Sands," *Computers and Geotechnics* 171 (2024): 106314, https://doi.org/10.1016/j.compgeo.2024.106314.

67. T. Benz, R. Schwab, and P. Vermeer, "Small–Strain Stiffness in Geotechnical Analyses," *Bautechnik* 86, no. S1 (2009): 16–27, https://doi.org/10.1002/bate.200910038.

68. D. Mašín and J. Duque, "Excavation of Komořany Tunnel in Sand: A Case Study," *International Journal of Geomechanics* 23, no. 8 (2023): 05023006, https://doi.org/10.1061/IJGNAI.GMENG-8591.

69. B. Simpson, "Retaining Structures: Displacement and Design," *Géotechnique* 42, no. 4 (1992): 541–576, https://doi.org/10.1680/geot.1992.42.4.541.

70. G. Gudehus and D. Mašín, "Graphical Representation of Constitutive Equations," *Géotechnique* 59, no. 2 (2009): 147–151, https://doi.org/10.1680/geot.2007.00155.

71. A. Niemunis, K. Nübel, and C. Karcher, "The Consistency Conditions for Density Limits of Hypoplastic Constitutive Law," *Task Quarterly* 4 (2000): 412–420.

72. E. Bauer, "Analysis of Shear Band Bifurcation With a Hypoplastic Model for a Pressure and Density Sensitive Granular Material," *Mechanics of Materials* 31, no. 9 (1999): 597–609, https://doi.org/10.1016/S0167-6636(99)00017-4.

73. D. Kolymbas and G. Rombach, "Shear Band Formation in Generalized Hypoelasticity," *Archive of Applied Mechanics* 59, no. 3 (1989): 177–186, https://doi.org/10.1007/bf00532248.

74. W. Wu, "Non-Linear Analysis of Shear Band Formation in Sand," *International Journal for Numerical and Analytical Methods in Geomechanics* 24, no. 3 (2000): 245–263, https://doi.org/10.1002/(SICI)1096-9853(200003)24:3⟨245::AID-NAG52⟩3.0.CO;2-C.

75. W. Wu and Z. Sikora, "Localized Bifurcation in Hypoplasticity," *International Journal of Engineering Science* 29, no. 2 (1991): 195–201, https://doi.org/10.1016/0020-7225(91)90016-V.

76. J. Tejchman and A. Niemunis, "FE-Studies on Shear Localization in an Anistropic Micro-Polar Hypoplastic Granular Material," *Granular Matter* 8, no. 3-4 (2006): 205–220, https://doi.org/10.1007/s10035-006-0009-z.

77. J. Tejchman and W. Wu, "Numerical Simulation of Shear Band Formation With a Hypoplastic Constitutive Model," *Computers and Geotechnics* 18, no. 1 (1996): 71–84, https://doi.org/10.1016/0266-352X(95)00018-6.

78. F. Collin, Y. Sieffert, and R. Chambon, *Mechanics of Unsaturated Geomaterials*, 1st ed. (Wiley and ISTE, 2010).

79. D. R. Borst, "Numerical Modelling of Bifurcation and Localisation in Cohesive-Frictional Materials," *Pure and Applied Geophysics* 137, no. 4 (1991): 367–390, https://doi.org/10.1007/BF00879040.

Appendix A: Notation

The conventional mechanical sign convention is used throughout this paper. Extension strain and tensile stress are positive. Second-order tensors are written in bold letters (e.g., $\boldsymbol{\sigma}$ or $\boldsymbol{m}$), with $\| \sqcup \|$ denoting the Euclidean norm and $\mathrm{tr}(\sqcup)$ representing the sum of diagonal components of the corresponding second-order tensor $\sqcup$. The deviatoric part is denoted with $\sqcup^*$. Normalized tensors are denoted as $\vec{\sqcup} = \sqcup / \| \sqcup \|$ and the definition of the Mccauley brackets is $\langle x \rangle = (\sqcup + | \sqcup |)/2$. Fourth-order tensors are symbolized using capital sans-serif letters (e.g., E). The **symbol** $\cdot$ denotes multiplication with one dummy index (single contraction). The multiplication with two dummy indices (double contraction) is written using a colon, for example, $\boldsymbol{a} : \boldsymbol{b}$. Dyadic multiplication is written as $\boldsymbol{ab}$. A list of symbols is provided in Table A1.

TABLE A1 | List of symbols.

$\boldsymbol{\sigma}$	effective tress tensor (tension positive)
e	void ratio
$\boldsymbol{h}$	intergranular strain tensor
$\boldsymbol{z}$	fabric/Structure tensor
Ω	cyclic preloading variable
$\boldsymbol{\alpha}$	additional state variables
$\boldsymbol{\varepsilon}$	strain tensor (compression negative)
$\dot{\boldsymbol{\sigma}}$	effective stress rate
$\dot{\boldsymbol{\varepsilon}}$	strain rate
$p = -\mathrm{tr}(\boldsymbol{\sigma})/3$	roscoe mean effective pressure
$q = \|\boldsymbol{\sigma}^*\|\sqrt{3/2} \overset{triax}{=} \sigma_r - \sigma_a$	roscoe deviatoric stress
$P = -\mathrm{tr}(\boldsymbol{\sigma})/\sqrt{3}$	isometric mean effective pressure

(Continues)

TABLE A1 | (Continued)

$Q = \|\boldsymbol{\sigma}^*\|$	isometric deviatoric stress
$\dot{\varepsilon}_{\text{vol}} = -\operatorname{tr}(\dot{\boldsymbol{\varepsilon}})$	volumetric strain rate
$\dot{\varepsilon}_P = -\operatorname{tr}(\dot{\boldsymbol{\varepsilon}})/\sqrt{3}$	isometric volumetric strain rate
$\dot{\varepsilon}_Q = \|\dot{\boldsymbol{\varepsilon}}^*\|$	isometric deviatoric strain rate
$I_D = (e_{c0} - e)/(e_{c0} - e_{d0})$	relative density
$\boldsymbol{\delta}$	unit tensor of second order (Kronecker symbol)
I	symmetrizing unit tensor of fourth order
$\mathsf{E}, \overline{\mathsf{E}}, \overline{\mathsf{E}}^{\diamond}$	Elastic stiffness tensor
C	compliance tensor
S	state mobilization
Y	degree of nonlinearity
Y_z	degree of additional nonlinearity due to fabric effects
Y_d	degree of additional dilatancy to avoid too dense states
C	scalar value introduced in the extended generalized hypoplasticity
$\boldsymbol{m}, \boldsymbol{m}^a, \boldsymbol{m}^c, \boldsymbol{m}^i$	hypoplastic equivalent flow rule and explicit defined parts of it
$\boldsymbol{m}^z$	direction of additional irreversible deformations due to fabric effects
$\boldsymbol{m}^d$	direction of additional dilatancy to avoid too dense states
Tables 1–3	symbols denoting the constitutive parameters

Appendix B: Equations of NHP

The equations of neohypoplasticity (NHP) are summarized below. Note that the governing equations of the coupled NHP+GIS model are obtained from the following equations and those in Section 4:

Stress rate

$$\dot{\boldsymbol{\sigma}} = \overline{\mathsf{E}} : \left(\dot{\boldsymbol{\varepsilon}} - \boldsymbol{m}Y\|\dot{\boldsymbol{\varepsilon}}\| - \boldsymbol{m}^z Y_z\|\dot{\boldsymbol{\varepsilon}}\| - \boldsymbol{m}^d Y_d\|\dot{\boldsymbol{\varepsilon}}\|\right) \tag{B1}$$

Hyperelastic stiffness

$$\bar{\psi}(\boldsymbol{\sigma}) = \sum_{\alpha} P_0\, c\left(\frac{P}{P_0}\right)^{\alpha}\left(\frac{R}{P_0}\right)^{2-n-\alpha} \quad \text{with} \quad \alpha \in \mathcal{R} \tag{B2}$$

$$R = \|\boldsymbol{\sigma}\| \quad \text{and} \quad P = -\operatorname{tr}(\boldsymbol{\sigma})/\sqrt{3} \tag{B3}$$

$$\bar{\psi}(\boldsymbol{\sigma}) = P_0\, c\left(\frac{P}{P_0}\right)^{\alpha}\left(\frac{R}{P_0}\right)^{2-n-\alpha} \tag{B4}$$

$$\frac{\partial^2 \bar{\psi}}{\partial\sigma_{ij}\partial\sigma_{kl}} = C_{ijkl} = (E_{ijkl})^{-1} \tag{B5}$$

Rotation of the hyperelastic stiffness

$$\begin{aligned} R_{ijkl} =& I_{ijkl} + (\cos\beta - 1)\left(u_{ij}u_{kl} + v_{ij}v_{kl}\right) \\ & - \sqrt{1-(\cos\beta)^2}\left(u_{ij}v_{kl} - v_{ij}u_{kl}\right) \end{aligned} \tag{B6}$$

$$u_{ij} = -\vec{\delta}_{ij} \qquad v_{ij} = \vec{z}_{ij} \tag{B7}$$

$$A_{ijkl} = \vec{\delta}_{ij}\vec{\delta}_{kl} \qquad D_{ijkl} = I_{ijkl} - A_{ijkl} \tag{B8}$$

$$\beta = \left(\frac{\|\boldsymbol{z}\|}{z_{\max}}\right)^{n_L} \begin{cases} \beta_L \frac{e - e_c(P)}{e_i(P) - e_c(P)} & \text{for } e > e_c(P) \\ \beta_D \frac{e_c(P) - e}{e_c(P) - e_d(P)} & \text{for } e < e_c(P) \end{cases} \tag{B9}$$

$$\overline{\mathsf{E}}^{\diamond} = \mathsf{A} : \mathsf{E} + \mathcal{R} : \mathsf{D} : \mathsf{E} = (\mathsf{A} + \mathcal{R} : \mathsf{D}) : \mathsf{E} \tag{B10}$$

Pyknotropy factor

$$F_e(e) = 1 + k_e\left\langle \frac{e_c(P) - e}{e_c(P) - e_d(P)} \right\rangle \tag{B11}$$

$$\overline{\mathsf{E}} = F_e(e)\,\overline{\mathsf{E}}^{\diamond} \tag{B12}$$

Pressure-dependent limit void ratios

$$\frac{e_i}{e_{i0}} = \frac{e_d}{e_{d0}} = \frac{e_c}{e_{c0}} = \exp\left[-\left(\frac{\sqrt{3}P}{h_s}\right)^{n_B}\right] \tag{B13}$$

Degree of nonlinearity

$$H(\boldsymbol{\sigma}) = \operatorname{tr}(\boldsymbol{\sigma})\operatorname{tr}(\boldsymbol{\sigma}^{-1}) - 9 \quad \in (0, \infty) \tag{B14}$$

$$F_{\text{MN}}(\boldsymbol{\sigma}) = H(\boldsymbol{\sigma}) - H_{\max} \le 0 \tag{B15}$$

$$H_{\max}(\varphi) = 8\tan^2[\varphi] \tag{B16}$$

$$\varphi(e) = \varphi_c + \begin{cases} (\varphi_d - \varphi_c)\frac{e_c(P) - e}{e_c(P) - e_d(P)} & \text{for } e < e_c(P) \\ (\varphi_i - \varphi_c)\frac{e - e_c(P)}{e_i(P) - e_c(P)} & \text{for } e > e_c(P) \end{cases} \tag{B17}$$

$$Y(x) = A_Y \exp\left(\frac{-1}{B_Y x^{n_Y} + C_Y}\right) \tag{B18}$$

$$x = \frac{H}{H_{\max}(\varphi)} \tag{B19}$$

$$A_Y = \exp\left(\frac{1}{B_Y + C_Y}\right) \tag{B20}$$

Hypoplastic equivalent flow rule

$$\varphi_{\text{PT}}(e) = \varphi_c + (\varphi_i - \varphi_c)\left\langle \frac{e_c(P) - e}{e_c(P) - e_d(P)} \right\rangle \tag{B21}$$

$$m_{ij} = \begin{cases} m^a_{ij} = \left[\delta_{ij}\sigma^{-1}_{kk} - \sigma_{kk}\sigma^{-2}_{ij}\right]^{\rightarrow} & \text{if } \frac{H(\boldsymbol{\sigma})}{H_{\max}(\varphi_a)} \ge 1 \\ m^c_{ij} = \left(\left[\delta_{ij}\sigma^{-1}_{kk} - \sigma_{kk}\sigma^{-2}_{ij}\right]^{*}\right)^{\rightarrow} & \text{if } \frac{H(\boldsymbol{\sigma})}{H_{\max}(\varphi_{\text{PT}})} = 1 \\ m^i_{ij} = -\left(\delta_{ij}\right)^{\rightarrow} & \text{if } H = 0 \end{cases} \tag{B22}$$

$$\begin{aligned} \boldsymbol{m} &= \left[y\boldsymbol{m}^c + (1-y)\boldsymbol{m}^i\right]^{\rightarrow} \quad \text{for } y = \left(\frac{H(\boldsymbol{\sigma})}{H_{\max}(\varphi_{\text{PT}})}\right)^{n_1} \\ \boldsymbol{m} &= \left[y\boldsymbol{m}^a + (1-y)\boldsymbol{m}^c\right]^{\rightarrow} \quad \text{for } y = \left(\frac{H(\boldsymbol{\sigma}) - H_{\max}(\varphi_{\text{PT}})}{H_{\max}(\varphi_a) - H_{\max}(\varphi_{\text{PT}})}\right)^{n_2} \end{aligned} \tag{B23}$$

Additional contractancy due to fabric

$$Y_z = \omega(z_{\max} - \boldsymbol{z} : \vec{\dot{\boldsymbol{\varepsilon}}}) \tag{B24}$$

$$\omega(e) = \frac{P_z}{z_{\max}(100P_0 + P)}\, f_{ac}(e) \tag{B25}$$

$$f_{ac}(e) = 1 - \frac{1}{1 + \exp\left(k_d(e - e_d(P))\right)} \tag{B26}$$

$$\dot{\boldsymbol{z}} = A_z\left(\dot{\boldsymbol{\varepsilon}}^{\diamond} - \vec{\boldsymbol{z}}\left(\frac{\|\boldsymbol{z}\|}{z_{\max}}\right)^{\beta_z} \|\dot{\boldsymbol{\varepsilon}}^{\diamond}\|\right)\left(\alpha_z + \left(\frac{\|\boldsymbol{z}\|}{z_{\max}}\right)^{n_z}\right) \tag{B27}$$

$$\dot{\boldsymbol{\varepsilon}}^{\diamond} = \left(\frac{\dot{\varepsilon}_Q^2}{\dot{\varepsilon}_Q^2 + \dot{\varepsilon}_P^2}\right)^{10} \dot{\boldsymbol{\varepsilon}}^{*} \tag{B28}$$

$$A_z = \frac{F_e\, u_z}{c\,(2 - n - \alpha)(P/P_0)^{1-n}} \tag{B29}$$

$$\boldsymbol{m}^z = \vec{\boldsymbol{\sigma}} \tag{B30}$$

Additional dilatancy for $e < e_d$

$$Y_d = f_{\text{ad}}\, Y_{\text{dd}} = f_{\text{ad}}\left(Y + 1 - a\left(\frac{P}{P_0}\right)^{1-n_B} \frac{1 + e_d(P)}{\overline{E}_{PP}\; a\; n_B\; e_d(P)}\right) \tag{B31}$$

$$\overline{E}_{PP} = (\delta_{ij}\overline{E}_{ijkl})\delta_{kl}/\sqrt{3} \;\text{ and }\; a = \sqrt{3}/h_s \tag{B32}$$

$$f_{\text{ad}} = 1 - \frac{1}{1 + \exp\left(k_d(e_d(P) - e)\right)} \tag{B33}$$

$$\boldsymbol{m}^d = \vec{\boldsymbol{\delta}} \tag{B34}$$

Void ratio evolution

$$\dot{e} = (1 + e)\,\mathrm{tr}(\dot{\boldsymbol{\varepsilon}}) \tag{B35}$$

Appendix C: Artificial Accumulation

The phenomenon of an artificial accumulation [31] in hypoelastic constitutive models is demonstrated using the linear part L_{ijkl} of HP. For the mathematical expression, it is referred to the literature [9]. The resulting model is hypoelastic and can be written as follows:

$$\dot{\sigma}_{ij} = L_{ijkl}\,\dot{\varepsilon}_{kl}. \tag{C1}$$

The hyperelastic constitutive formulation

$$\dot{\sigma}_{ij} = E_{ijkl}\,\dot{\varepsilon}_{kl} \tag{C2}$$

using the hyperelastic stiffness from NHP, see Equation (B5), is considered for comparison. The hypoelastic stiffness L_{ijkl} and the hyperelastic stiffness E_{ijkl} are functions of the effective stress only, and therefore the effective stress is the only state variable in both constitutive formulations.

A triaxial stress state with $\sigma_{a0}/2 = \sigma_{r0} = -200$ kPa is considered. Closed triaxial strain cycles (expressed ε_P and ε_Q) are considered. Note that the strain path was scaled to generate comparable stress amplitudes.

The stress component σ_r as a function of the number of closed strain cycles N is shown in Figure C1a for the hypoelastic and in Figure C1b for the hyperelastic formulation. It is evident that in a hypoelastic model, an artificial stress accumulation may occur, whereas the latter is prevented in a hyperelastic model. It follows that a constitutive model with a hyperelastic stiffness should be used to simulate the soil behavior under cyclic deformations. NHP or the model [11] fulfills this requirement, while HP does not.

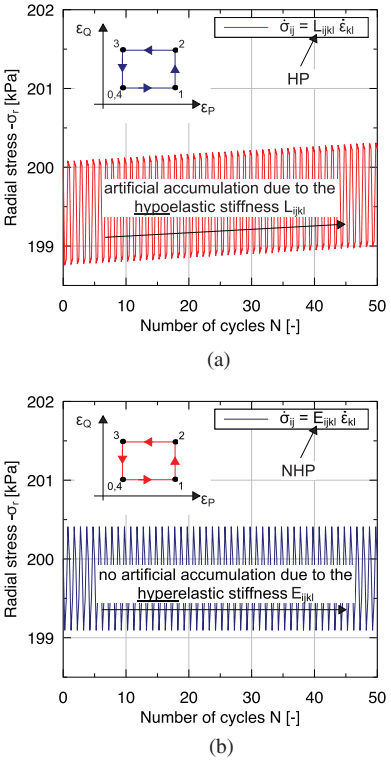

FIGURE C1 | Closed strain cycles can result in (a) an artificial accumulation of stress using a hypoelastic constitutive model, whereas artificial accumulation do not occur in (b) a hyperelastic constitutive model.